CENTRAL REGIONS OF BARRED GALAXIES: TWO-DIMENSIONAL NON-SELF-GRAVITATING HYDRODYNAMIC SIMULATIONS

Woong-Tae Kim[1,2,3], Woo-Young Seo[1,2], James M. Stone[4], Doosoo Yoon[2,5], and Peter J. Teuben[6]

[1] Center for the Exploration of the Origin of the Universe (CEOU), Astronomy Program, Department of Physics and Astronomy, Seoul National University, Seoul 151-742, Republic of Korea; wkim@astro.snu.ac.kr

[2] FPRD, Department of Physics and Astronomy, Seoul National University, Seoul 151-742, Republic of Korea

[3] Institute for Advanced Study, Einstein Drive, Princeton, NJ 08540, USA

[4] Department of Astrophysical Sciences, Princeton University, Princeton, NJ 08544, USA

[5] Department of Astronomy, University of Wisconsin–Madison, Madison, WI 53706, USA

[6] Department of Astronomy, University of Maryland, College Park, MD 20742, USA

ABSTRACT

The inner regions of barred galaxies contain substructures such as off-axis shocks, nuclear rings, and nuclear spirals. These substructures may affect star formation, and control the activity of a central black hole (BH) by determining the mass inflow rate. We investigate the formation and properties of such substructures using high-resolution, grid-based hydrodynamic simulations. The gaseous medium is assumed to be infinitesimally thin, isothermal, and non-self-gravitating. The stars and dark matter are represented by a static gravitational potential with four components: a stellar disk, a bulge, a central BH, and a bar. To investigate various galactic environments, we vary the gas sound speed, c_s, as well as the mass of the central BH, M_{BH}. Once the flow has reached a quasi-steady state, off-axis shocks tend to move closer to the bar major axis as c_s increases. Nuclear rings shrink in size with increasing c_s, but are independent of M_{BH}, suggesting that the ring position is not determined by the Lindblad resonances. Rings in low-c_s models are narrow since they are occupied largely by gas on x_2-orbits and well decoupled from nuclear spirals, while they become broad because of large thermal perturbations in high-c_s models. Nuclear spirals persist only when either c_s is small or M_{BH} is large; they would otherwise be destroyed completely by the ring material on eccentric orbits. The shape and strength of nuclear spirals depend sensitively on c_s and M_{BH} such that they are leading if both c_s and M_{BH} are small, weak trailing if c_s is small and M_{BH} is large, and strong trailing if both c_s and M_{BH} are large. While the mass inflow rate toward the nucleus is quite small in low-c_s models because of the presence of a narrow nuclear ring, it becomes larger than 0.01 $M_\odot$ yr^{-1} when c_s is large, providing a potential explanation of nuclear activity in Seyfert galaxies.

Key words: galaxies: ISM – galaxies: kinematics and dynamics – galaxies: nuclei – galaxies: spiral – hydrodynamics – ISM: general – shock waves

Online-only material: color figures

1. INTRODUCTION

Stellar bars play an important role in the dynamical evolution of gas in galaxies. By introducing a non-axisymmetric torque, they produce interesting morphological substructures in the gaseous medium, including a pair of dust lanes at the leading side of the bar, a nuclear ring near the center, and nuclear spirals inside the ring (e.g., Sanders & Huntley 1976; Roberts et al. 1979; Schwarz 1981; van Albada & Roberts 1981; Athanassoula 1992b; Piner et al. 1995; Buta & Combes 1996; Martini et al. 2003a, 2003b; Martinez-Valpuesta et al. 2006). They also transport gas inward which can trigger starbursts in the rings (e.g., Buta 1986; Garcia-Barreto et al. 1991; Heller & Shlosman 1994; Barth et al. 1995; Maoz et al. 2001; Mazzuca et al. 2008) and if the mass inflow extends all the way to the center, they may help power active galactic nuclei (AGNs; e.g., Shlosman et al. 1990; Regan & Mulchaey 1999; Knapen et al. 2000; Laurikainen et al. 2004; van de Ven & Fathi 2010).

Since bar substructures represent a nonlinear response of the gas to a non-axisymmetric gravitational potential, their formation and evolution is best studied using direct numerical simulations.[7] There have been a number of numerical studies

on the gas dynamics in barred galaxies. Based on the numerical scheme employed, they can be categorized largely into two groups: (1) those using a smoothed particle hydrodynamics (SPH) technique (e.g., Englmaier & Gerhard 1997; Patsis & Athanassoula 2000; Ann & Thakur 2005; Thakur et al. 2009) and (2) those using a grid-based algorithm (e.g., Athanassoula 1992b; Piner et al. 1995; Maciejewski et al. 2002; Maciejewski 2004b; Regan & Teuben 2003, 2004). The numerical results from these two approaches do not always agree with each other, at least quantitatively, even if the model parameters are almost identical. For instance, Piner et al. (1995) using the CMHOG code on a cylindrical grid reported that the gas near the corotation regions exhibits complex density features resulting from Rayleigh–Taylor and/or Kelvin–Helmholtz instabilities, while these structures are absent in the SPH simulations. In addition, overall shapes and structures of dust lanes and nuclear rings from CMHOG simulations are different from SPH results.

Some differences in the numerical results may be attributable to relatively large numerical diffusion of a standard SPH method and its inability to handle sharp discontinuities accurately (e.g., Agertz et al. 2007; Price 2008; Read et al. 2010). However, after adopting and thoroughly testing the CMHOG code as part of this work, we have found that it contained a serious bug in the way the gravitational forces due to the bar are added to the hydrodynamical equations. Thus, some of the discrepancies in

---

[7] Englmaier & Shlosman (2000) argued that physical properties of nuclear spirals can be explained by the linear density-wave theories (see also Maciejewski 2004a).

the flows computed by CMHOG and other codes are likely due to this bug. We discuss this bug and its effect on the results reported in Piner et al. (1995) in Section 2.2.

In this paper, we revisit the gas dynamics in barred galaxies using a corrected version of the CMHOG code. Our objectives are three-fold. First, we wish to remedy the errors in Piner et al. (1995) and to compute the formation of bar substructures with an accurate shock-capturing grid code with the correct bar potential. Second, the morphology, shape, and strength of the bar substructures are likely to depend on the gas sound speed and the shape of the underlying gravitational potential (e.g., Englmaier & Shlosman 2000). Thus, we report new models in which we include a central black hole (BH) that greatly affects the gravitational potential in the central regions, and we vary both the BH mass and the sound speed to explore the dynamics in various galactic conditions. Third, we exploit advances in computational resources to compute models that have more than an order of magnitude higher resolution than the models in Piner et al. (1995), with a grid resolution of 0.13 pc in the central regions. This allows us to resolve details in the flow in the nuclear regions, in particular the formation of nuclear rings and nuclear spirals.

According to the most widely accepted theory, a nuclear ring forms near the inner Lindblad resonance (ILR) when there is only one ILR, as the gas outside (inside) ILR loses (gains) angular momentum and accumulates there, while it forms in between the inner ILR and outer ILR when there are two ILRs (e.g., Shlosman et al. 1990; Combes 1996; Buta & Combes 1996). On the other hand, Regan & Teuben (2003) argued that the ring formation is more deeply related to the existence of x_2-orbits rather than the ILRs. But the arguments relying on either ILRs or x_2-orbits do not take into account the effect of thermal pressure. Therefore, it is important to explore to what extent the concepts of ILRs or x_2-orbits are valid in describing nuclear rings, especially when the sound speed is large.

The formation, shape, and nature of nuclear spirals that may channel the gas to the galaxy centers are also not well understood. Observations using the *Hubble Space Telescope* indicate that galaxies having nuclear dust spirals are quite common (e.g., Martini et al. 2003a, 2003b). While most such spirals are trailing, a few galaxies including NGC 1241 and NGC 6902 reportedly possess leading nuclear spirals (Díaz et al. 2003; Grosbøl 2003). Although the linear theory suggests that leading spirals are expected when there are two ILRs (e.g., Maciejewski 2004a), they are absent in the numerical models of Piner et al. (1995) computed with the CMHOG code, while the SPH models of Ann & Thakur (2005) with self-gravity do form leading spirals. The SPH models suffer from poor spatial resolution at the nuclear regions as most particles gather around the rings. By running high-resolution simulations with a corrected version of CMHOG, we can clarify the issues of the nuclear spiral formation and related mass inflow rates to the galaxy center.

In this work we treat gaseous disks as being two dimensional, isothermal, non-self-gravitating, and unmagnetized, which introduces a few caveats that need be noted from the outset. By considering an infinitesimally thin disk, we ignore gas motions and associated dynamics along the direction perpendicular to the disk. By imposing a point symmetry relative to the galaxy center, our models do not allow for the existence of odd-m modes, although this appears reasonable since $m = 2$ modes dominate in the problems involving a galactic bar. In addition, we are unable to capture the potential consequences of gaseous

self-gravity and magnetic stress that may not only cause fragmentation of high-density nuclear rings but also affect mass inflow rates to the galaxy center. Nevertheless, these idealized models are useful to isolate the effects of the gas sound speed and the mass of a central BH on the formation of bar substructures and mass inflows. Also, these models allow us to correct the results of previous CMHOG calculations with incorrect bar forces.

This paper is organized as follows. In Section 2, we describe the galaxy model, model parameters, and our numerical methods. In Section 3, we present the results of simulations for off-axis shocks and nuclear rings. The detailed properties of nuclear spirals are presented in Section 4. In Section 5, we study the mass inflow rates through the inner boundary obtained from our simulations. In Section 6, we conclude with a summary and discussion of our results and their astronomical implications.

2. MODELS AND METHODS

We consider a uniform, isothermal, infinitesimally thin, and non-self-gravitating gas disk orbiting in a gravitational potential $\Phi_{\rm ext}$ arising from various components of a barred galaxy. The bar is assumed to rotate about the galaxy center with a fixed pattern speed $\mathbf{\Omega_b} = \Omega_b\hat{\mathbf{z}}$. Therefore, it is advantageous to solve the dynamical equations in cylindrical polar coordinates (R, ϕ) corotating with the bar in the $z = 0$ plane. The equations of ideal hydrodynamics in this rotating frame are

$$\left(\frac{\partial}{\partial t} + \mathbf{u} \cdot \nabla\right)\Sigma = -\Sigma\nabla \cdot \mathbf{u}, \tag{1}$$

$$\left(\frac{\partial}{\partial t} + \mathbf{u} \cdot \nabla\right)\mathbf{u} = -c_s^2\frac{\nabla\Sigma}{\Sigma} - \nabla\Phi_{\rm ext} + \Omega_b^2\mathbf{R} - 2\mathbf{\Omega_b} \times \mathbf{u}, \tag{2}$$

where Σ, $\mathbf{u}$, and c_s denote the surface density, velocity in the rotating frame, and the sound speed in the gas, respectively. The third and fourth terms on the right-hand side of Equation (2) represent the centrifugal and Coriolis forces, respectively, arising from the coordinate transformation from the inertial to rotating frames. The velocity $\mathbf{v}$ in the inertial frame is obtained from $\mathbf{v} = \mathbf{u} + R\Omega_b\hat{\phi}$. In order to focus on the bar-driven gas dynamics, we do not consider star formation and the associated gas recycling in the present work.

The external gravitational potential $\Phi_{\rm ext}$ consists of four components: an axisymmetric stellar disk, a spherical bulge, a non-axisymmetric bar, and a central supermassive BH. The Appendix describes the specific potential model we employ for each component of the galaxy. The bar pattern speed is taken to be $\Omega_b = 33$ km s^{-1} kpc^{-1}. Without a central BH, our galaxy model is similar to those in Athanassoula (1992a, 1992b) and Piner et al. (1995). The presence of a BH allows us to explore the effect of central mass concentration on the formation of nuclear spirals (e.g., Maciejewski 2004b; Thakur et al. 2009).

2.1. Models

The real interstellar gas is multiphase and turbulent, with temperatures differing by a few orders of magnitude (e.g., Field et al. 1969; McKee & Ostriker 1977, 2007). For simplicity, we model this highly inhomogeneous gas using an isothermal equation of state with an effective sound speed c_s that includes a contribution due to turbulent motions. We have calculated 15 different models in which we vary both c_s and the initial mass $M_{\rm BH}(0)$ of the central BH as parameters. Table 1 lists the

Table 1
Model Parameters

Model	c_s(km s^{-1})	$M_{BH}(0)$ ($M_\odot$)
cs05bh0	5	0
cs05bh0t[a]	5	0
cs10bh0	10	0
cs15bh0	15	0
cs20bh0	20	0
cs20bh0t[a]	20	0
cs05bh7	5	4×10^7
cs10bh7	10	4×10^7
cs15bh7	15	4×10^7
cs20bh7	20	4×10^7
cs20bh7t[a]	20	4×10^7
cs05bh8	5	4×10^8
cs10bh8	10	4×10^8
cs15bh8	15	4×10^8
cs20bh8	20	4×10^8

Note. [a] The BH mass is varied with time as $M_{BH}(t) = M_{BH}(0) + \int_0^t \dot{M}(t')dt'$ assuming that all the inflowing mass is added to the central BH.

Figure 1. Rotational velocity of each component of the model galaxy with a central BH of $M_{BH} = 4 \times 10^8 \, M_\odot$. The solid and dashed lines are for along the bar major and minor axes, respectively. Note that the effect of the BH is almost negligible at $R > 1$ kpc, while it dominates the total gravitational potential at $R \lesssim 0.1$ kpc.
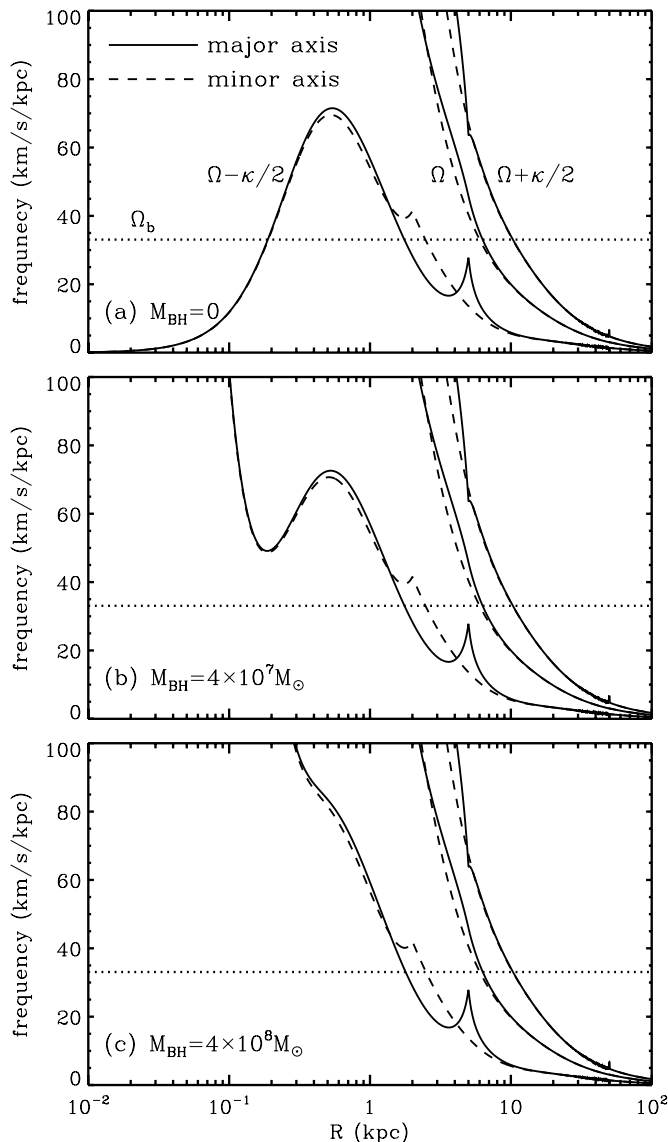
properties of each calculation. The sound speed is chosen to vary between 5 and 20 km s^{-1}. Models with a postfix bh0 do not initially possess a central BH, and are similar to those in Piner et al. (1995). Models with the postfix bh7 or bh8 have a BH with mass $M_{BH}(0) = 4 \times 10^7 \, M_\odot$ and $4 \times 10^8 \, M_\odot$, respectively; they are analogous to models in Maciejewski (2004b) and Ann & Thakur (2005). For most models, we fix the BH mass to its initial value, but we also consider three additional models (cs05bh0t, cs20bh0t, and cs20bh7t) in which the BH mass is varied with time according to $M_{BH}(t) = M_{BH}(0) + \int_0^t \dot{M}(t')dt'$, where $\dot{M}$ is the mass inflow rate across the inner boundary (see below). These time-varying M_{BH} models allow us to study the effect of BH growth due to the gas accretion on bar substructures.

Figure 1 plots the net circular rotation curves together with a contribution from each component when $M_{BH} = 4 \times 10^8 \, M_\odot$. The solid and dashed lines are along the bar major and minor axes, respectively. The circular velocity is almost flat at $\sim$200 km s^{-1} in the outer parts. Without the BH, the rotation curve v_c would rise linearly with R close to the center, but the presence of the BH results in $v_c \propto R^{-1/2}$ for $R \lesssim 0.1$ kpc. This rapid increase of v_c will render the gaseous orbits in the very central regions highly resistant to pressure perturbations, resulting in smaller mass inflow rates than the cases without it, as we show below.

Figure 2 shows the characteristic angular frequencies, $\Omega - \kappa/2$, Ω, and $\Omega + \kappa/2$ along the bar major and minor axes as solid and dashed lines, respectively.[8] Here, $\Omega^2 \equiv R^{-1}d\Phi_{ext}/dR$ and $\kappa^2 \equiv R^{-3}d(R^4\Omega^2)/dR$ denote the angular and epicyclic frequencies, respectively. The horizontal dotted line in each panel represents the bar pattern speed of $\Omega_b = 33$ km s^{-1} kpc^{-1}, with the corotation resonance (CR) located at $R_{CR} = 6$ kpc for all models. For bh0 models with no BH, the $\Omega - \kappa/2$ curve peaks at $R_{max} = 0.53$ kpc and is equal to Ω_b at the two ILRs with radii of $R_{IILR} = 0.19$ kpc and $R_{OILR} \approx 2$ kpc. Because

the rotation curve rises steeply toward the center, bh7 and bh8 models have only a single ILR at $R_{ILR} \approx 2$ kpc. The $\Omega - \kappa/2$ curve in bh7 models attains its local maximum and minimum at $R_{max} = 0.53$ kpc and $R_{min} = 0.19$ kpc, respectively. In bh8 models, on the other hand, it increases monotonically with decreasing R since the BH dominates the gravitational potential. We will show in Section 4 that the shape of nuclear spirals depends critically on the sign of $d(\Omega - \kappa/2)/dR$ (e.g., Buta & Combes 1996).

2.2. Numerical Methods

To solve Equations (1) and (2), we use the two-dimensional grid-based code CMHOG in cylindrical geometry (Piner et al. 1995). CMHOG implements the piecewise parabolic method in its Lagrangian remap formulation (Colella & Woodward 1984), which is third-order accurate in space and has very little numerical diffusion (viscosity). All the runs are carried out in a frame corotating with a bar whose major axis is aligned along the y-axis (i.e., $\phi = \pm\pi/2$), so that the bar potential remains stationary in the simulation domain. By assuming a reflection symmetry with respect to the galaxy center, the simulations were performed on a half-plane with $-\pi/2 \leqslant \phi \leqslant \pi/2$ constructed by making a cut along the bar major axis.

As mentioned in Section 1, the original version of CMHOG used by Piner et al. (1995) contained a serious bug in the way the gravitational forces were added to the hydrodynamic equations. The CMHOG code places a bar potential Φ_{bar} with the major axis aligned along the x-axis, calculates the bar forces $f_x = -\partial\Phi_{bar}/\partial x$ and $f_y = -\partial\Phi_{bar}/\partial y$, and then transforms them into cylindrical coordinates. In the original version of the code, the incorrect transform relations $f_R = f_x \cos\phi + f_y \sin\phi$ and $f_\phi = f_x \sin\phi - f_y \cos\phi$ were used. In fact, the correct transformation rule for the azimuthal force should be $f_\phi = -f_x \sin\phi + f_y \cos\phi$. With the sign of the

---
[8] In the presence of a non-axisymmetric bar potential, the concepts of Ω as an angular frequency and κ as a radial frequency do not apply strictly since closed orbits are in general non-circular. In our models, however, the bar potential is nearly axisymmetric at $R < 1$ kpc, so that Ω and κ measure the actual frequencies reasonably well in the central parts.

Figure 2. Angular frequencies of galaxy models with different BH masses. The solid and dashed lines represent $\Omega - \kappa/2$ (leftmost curves), Ω (middle curves), and $\Omega + \kappa/2$ (rightmost curves) along the bar major and minor axes, respectively. The dotted lines denote the bar pattern speed Ω_b. (a) Models without a BH have two ILRs at $R_{\mathrm{IILR}} = 0.19$ kpc and $R_{\mathrm{OILR}} \approx 2$ kpc, with the maximum of the $\Omega - \kappa/2$ curve occurring at $R_{\max} = 0.53$ kpc. (b) Models with $M_{\mathrm{BH}} = 4 \times 10^7 \, M_\odot$ have a single ILR at $R_{\mathrm{ILR}} \approx 2$ kpc, with the local maximum and minimum of the $\Omega - \kappa/2$ curve occurring at $R_{\max} = 0.53$ kpc and $R_{\min} = 0.19$ kpc. (c) Models with $M_{\mathrm{BH}} = 4 \times 10^8 \, M_\odot$ have a single ILR at $R_{\mathrm{ILR}} \approx 2$ kpc, with $d(\Omega - \kappa/2)/dR < 0$ in the nuclear regions with $R < 1$ kpc.

azimuthal force reversed (but the radial force correct), the flows in models computed using the original CMHOG code behave as if the bar potential were aligned parallel to the y-axis, but with forces quite different from the intended ones. Other than these force transformations, the complex hydrodynamic algorithms in CMHOG are all implemented correctly, and were well tested in the original paper by Piner et al. (1995). Therefore, previous numerical studies based on CMHOG should remain valid as long as they do not adopt the incorrect transformations of the bar forces inherited from Piner et al. (1995). Unfortunately, the results of Piner et al. (1995) were compromised by a trivial sign error in the coordinate transform relations for the bar forces.

Figure 3 compares the results for a typical simulation run with the original and corrected version of CMHOG. For this

test, the grid resolution is taken identical to that in Piner et al. (1995) with 251 and 154 zones in the radial and azimuthal directions, respectively. The figure plots the logarithm of the surface density at $t = 300$ Myr. Several differences are apparent. For example, the gas around the CR at $R = 6$ kpc in the left panel is largely evacuated and has corrugated streams linked to the ends of the bar major axis, whereas the CR region is relatively featureless in the right panel. The nuclear ring in the left panel is fairly smooth, while it is quite clumpy in the right panel. Most importantly, the very central region inside the ring is almost unperturbed in the left panel, while the right panel shows spiral structures in the central region. These differences suggest that the original CMHOG code is unable to properly model the flow in the central regions, especially weak nuclear spirals. We have also run the same model using other grid-based codes adopting Cartesian coordinates, such as TVD (Kim et al. 1999) and Antares (Yuan & Yen 2005) as well as the particle-based GADGET code (Springel et al. 2001), in all of which the bar forces are calculated by taking finite differences of Φ_{bar} rather than using f_x and f_y directly. The new version of the CMHOG code used in this work gives results which are much more similar to the results of these other codes, which gives us further confidence that the gravitational forces due to the bar are now being treated correctly.

To resolve the central regions accurately, we set up a non-uniform, logarithmically spaced cylindrical grid with 1024 radial zones extending from 0.02 kpc to 16 kpc and 480 azimuthal zones covering the half-plane. This makes the zones approximately square-shaped throughout the grid (i.e., $\Delta R = R\Delta\phi$). The resulting grid spacing is $\Delta R = 0.13$, 6, and 100 pc at the inner radial boundary, $R = 1$ kpc where nuclear rings typically form, and the outer radial boundary, respectively. This increases the resolution in the inner regions by over an order of magnitude, in comparison to the models presented in Piner et al. (1995). This level of grid resolution is crucial to resolve nuclear spiral structures within $R = 1$ kpc. We use outflow and continuous boundary conditions at the inner and outer radial boundaries, respectively, while the azimuthal boundaries are periodic. The gas crossing the inner boundary is considered lost from the simulation domain. We keep track of the total mass crossing the inner boundary in order to study the mass inflow rates into the galactic nucleus.

Each model starts from a uniform disk with surface density $\Sigma_0 = 10 \, M_\odot \, \mathrm{pc}^{-2}$ that is rotating in force balance with an axisymmetric gravitational potential without a bar. In order to avoid strong transients in the fluid flow caused by a sudden introduction of the bar, we slowly introduce the bar potential over one bar revolution time of $2\pi/\Omega_b = 186$ Myr. This is accomplished by increasing the bar central density ρ_{bar} linearly with time and decreasing the bulge central density ρ_{bul}, while keeping the net central density $\rho_{\mathrm{bar}} + \rho_{\mathrm{bul}}$ fixed. This ensures that the shape of the total gravitational potential Φ_{ext}, when averaged along the azimuthal direction, is unchanged with time. All the models are run until 500 Myr. This corresponds to 1.2×10^4 and 10 orbits at the inner and outer radial boundaries, respectively, for bh8 models with $M_{\mathrm{BH}} = 4 \times 10^8 \, M_\odot$.

3. RESULTS

We take Model cs05bh0 with $c_s = 5$ km s^{-1} and no BH as our standard model. The overall evolution of other models with different c_s and M_{BH} is qualitatively similar, although the properties of the nuclear features that form differ considerably from model to model. In this section, we first describe the
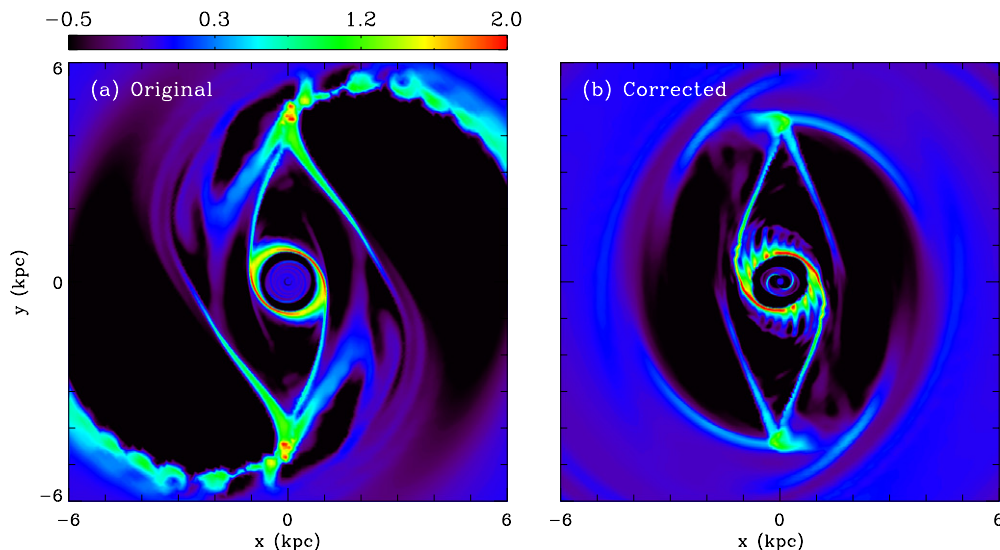
Figure 3. Logarithm of the gas surface density at $t = 300$ Myr from a test run using (a) the original CMHOG code and (b) the corrected version used in this work. A cylindrical grid with 251×154 zones is used. Compared to the left panel, gas in the right panel is relatively featureless in the corotation region at $R = 6$ kpc, has a more clumpy ring, and harbors nuclear spirals in the central region.

(A color version of this figure is available in the online journal.)

evolution of our standard model, and then present the differences in the off-axis shocks and nuclear rings caused by differing c_s and M_{BH}. The properties of nuclear spirals will be given in Section 4.

3.1. Overall Evolution

Figure 4 plots snapshots of the logarithm of the gas density at a few selected epochs in the inner regions of Model cs05bh0. The bar is oriented vertically along the y-axis, and the gas is rotating in the counterclockwise direction relative to the bar. The images extend to 6 kpc on either side of the center, corresponding to the CR radius, outside of which the gas remains almost unperturbed.[9] Piner et al. (1995) found that the CR regions exhibit time-dependent flow structures, as reproduced in Figure 3(a). On the other hand, Figure 4 shows that the CR regions in our simulations are quite stable and exhibit only at late time low-amplitude wavelike features entrained by the dense gas located at the bar ends, similar to the results of SPH simulations (e.g., Englmaier & Gerhard 1997; Patsis & Athanassoula 2000). This indicates that the complicated structures seen in Piner et al. (1995) were likely an artifact of the errors in their force transformation.

A striking feature of each of the snapshots shown in Figure 4 at times greater than 120 Myr is large amplitude oscillations in the density in the ring and dust lanes. These features are also seen in the simulations of Wada & Koda (2004) for spiral shocks, and are attributed to the "wiggle instability." As we will discuss below, this shock instability appears to be caused by vorticity generation in curved shocks.

An introduction of the non-axisymmetric bar potential induces perturbations on the gas orbits, causing them to deviate from circular trajectories. The gas density increases (decreases) in regions where neighboring orbits come close together (diverge). When $t = 60$ Myr, the overdense regions are preferentially located downstream from the bar major axis (Figure 4(a)). At this time, the overdensity produced by orbit crowding is largest at $R \sim 3$ kpc. Since the perturbing force by the bar is

weak inside $R \sim 1$ kpc, the overdensity there is correspondingly small and not readily discernible. Over time, the overdense regions become narrower and sharper as the bar amplitude grows and eventually develop into shock fronts at around $t = 100$ Myr. In what follows, we term these narrow shocks off-axis shocks.

A nuclear ring is beginning to shape at this time, as well. To illustrate the formation of nuclear rings in our models, we plot as solid lines in Figure 5 instantaneous streamlines of the gas that starts from Point A marked at $(x, y) = (1.5, -2.7)$ kpc in Model cs05bh0 and from $(x, y) = (1.4, -2.5)$ kpc in Model cs20bh0 with $c_s = 20$ km s^{-1} and no BH at $t = 100$ Myr. The two dotted circles in Figure 5(a) indicate the inner and outer ILRs at $R_{IILR} = 0.19$ kpc and $R_{OILR} = 2$ kpc. Note that the thick lines representing the overdense ridges in both models directly cross the outer ILR. The changes of the azimuthal and radial velocities along the streamlines are shown in Figures 5(b) and (c), where the dotted line indicates the equilibrium rotation curve of the model galaxy with no BH. On emerging from the overdense region (Point A), the gas moves radially inward on its epicycle orbit and increases (decreases) its azimuthal (radial) velocity due to the Coriolis force. It reaches Point B closest to the center when it attains $v_R = 0$ and largest v_ϕ. After this point, it moves radially outward, decreasing v_ϕ until it hits the off-axis shock at Point C. The gas loses a significant amount of angular momentum at the shock and begins to fall in. In addition, the shocked gas is swept by other shocked gas flowing from the bar-end regions along the shocks. Note that the shape of the off-axis shocks shown in Figure 5(a) coincides with the gas streamline from Points C to D, indicating that all the gas after crossing the shocks moves radially in along the shock fronts in the developing stage of the nuclear rings.

As the shocked gas moves along the shock fronts from Point C, it gradually rotates faster again. When the azimuthal velocity of the gas is increased to the level comparable to the equilibrium circular velocity at some radius R, it begins to follow a closed orbit (Point D), forming a nuclear ring at that radius. In other words, the centrifugal barrier inhibits the inflowing gas from moving further in. Regardless of the BH mass, this happens at $R \sim 0.8–1.2$ kpc in models with $c_s = 5$ km s^{-1} and

---

[9] The non-axisymmetric bar potential we adopt is very weak at $R > R_{CR}$.
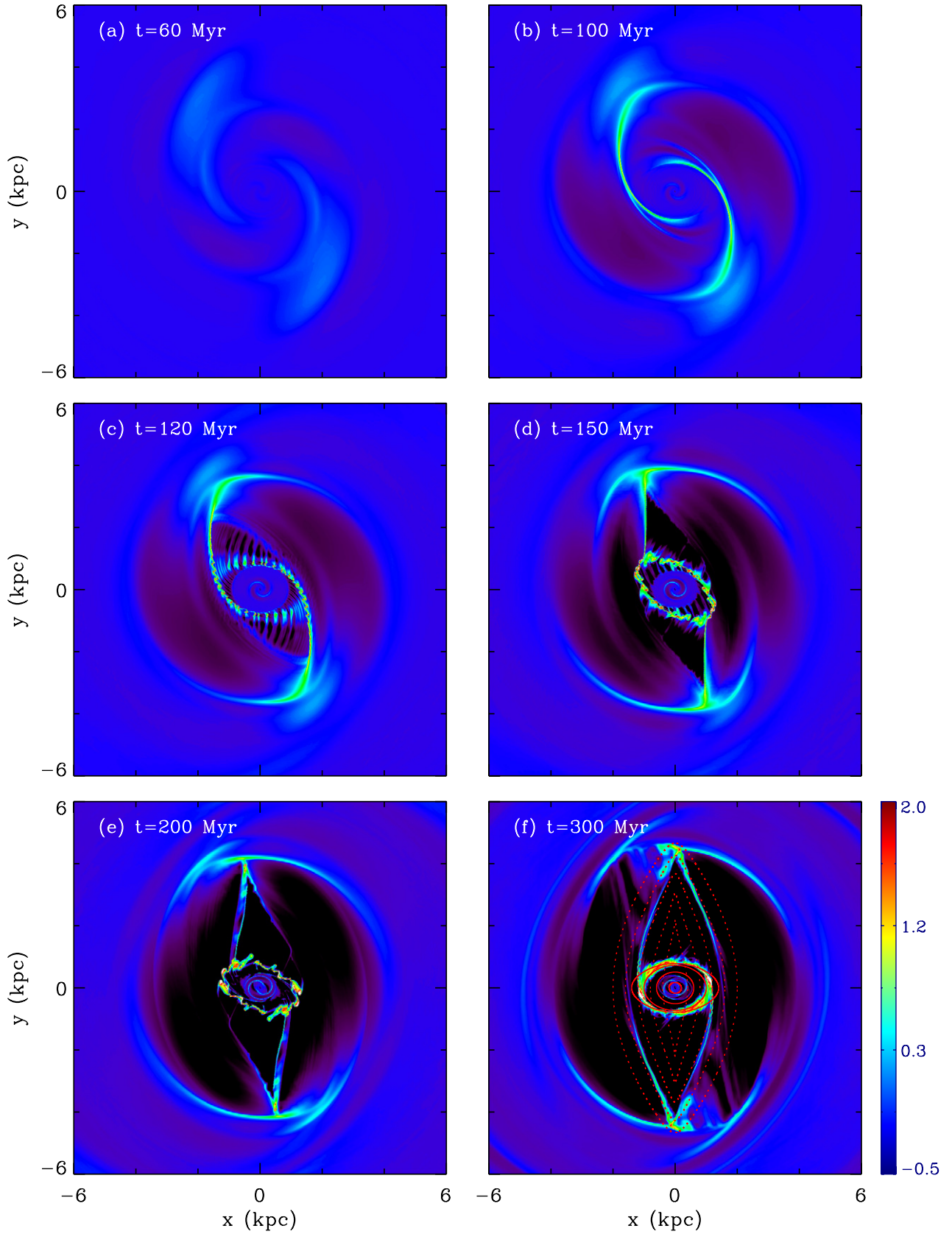
Figure 4. Snapshots of the logarithms of the gas surface density of Model cs05bh0. The bar is oriented vertically along the y-axis and remains stationary. The gas inside the CR is rotating in the counterclockwise direction. In (f), the dotted curves aligned vertically represent the x_1-orbits that cut the x-axis at $x_c = 0.4, 0.8, 1.2,$ and 1.6 kpc from inside to outside, while the solid curves aligned horizontally plot the x_2-orbits with $x_c = 0.2, 0.6, 1.0,$ and 1.4 kpc. Clumpy structures in (c)–(e) are produced by vortex generation at the curved shocks; see the text and Figure 6 for details.

(A color version of this figure is available in the online journal.)
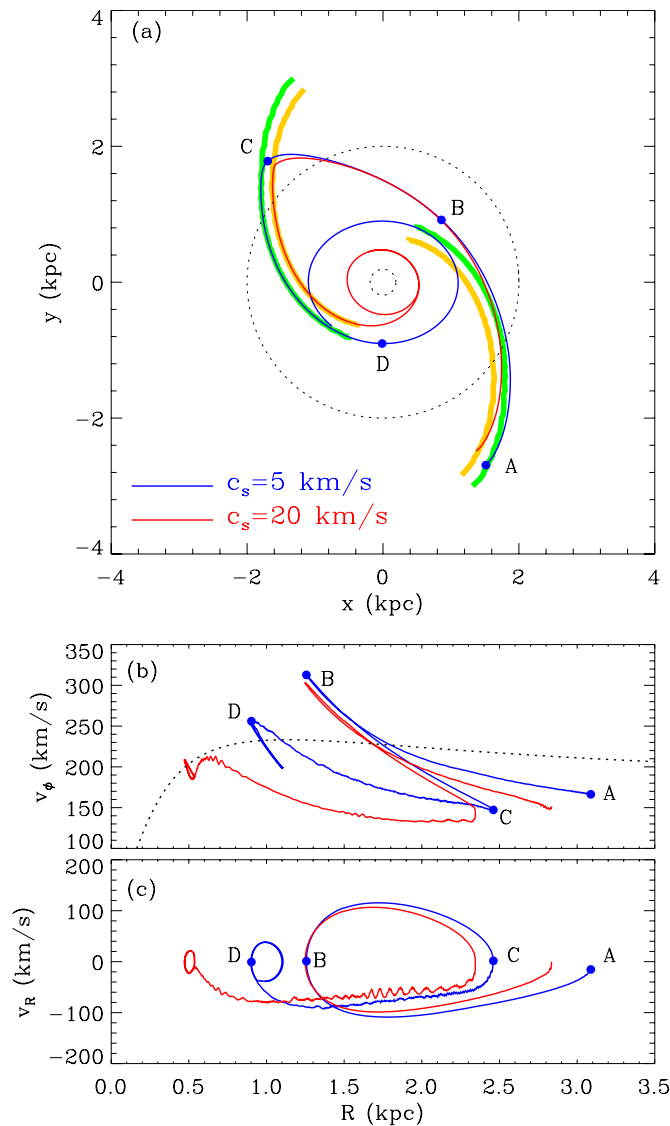
Figure 5. (a) Instantaneous streamlines of gas that starts from Point A $(x, y) = (1.5, -2.7)$ kpc in Model cs05bh0 and $(1.4, -2.5)$ kpc in Model cs20bh0 at $t = 100$ Myr. The thick green and orange curves represent the overdense ridges in Models cs05bh0 and cs20bh0, respectively. The two dotted circles indicate $R_{\mathrm{IILR}} = 0.19$ kpc and $R_{\mathrm{OILR}} = 2$ kpc. In Model cs05bh0, the gas reaches Point B closest to the galaxy center, is shocked at Point C, and forms a ring at Point D. (b and c) The variations of the azimuthal and radial velocities of the gas along the paths shown in (a). The initial equilibrium circular velocity is shown as a dotted line in (b).

(A color version of this figure is available in the online journal.)

$R \sim 0.4$–0.6 kpc in models with $c_s = 20$ km s^{-1} (Figures 4(b) and (c)). The facts that the off-axis shocks penetrate the ILR in bh7/bh8 models, the outer ILR in bh0 models, and that the ring positions are almost independent of M_{BH} when the rings are beginning to form suggest that the ring formation is unlikely to be governed by resonances. For models with low sound speed, the shape of nuclear rings is similar to an x_2-orbit. Clearly, the presence of the nuclear ring prevents the shocked gas from infalling directly to the nucleus.

Since the off-axis shocks are curved, Crocco's theorem ensures that vorticity can be generated at the shock fronts. Figure 6 plots snapshots of the potential vorticity $\xi \equiv |\nabla \times \mathbf{u} + 2\mathbf{\Omega}|/\Sigma$ relative to the initial value ξ_0 near the shocks at $t = 90$, 100, 110, and 120 Myr of the standard model. At $t = 90$ Myr, ξ/ξ_0 is largest along the shocks. Vorticity produced at the shocks is

advected with the background flows and enters the shock fronts at the opposite side after a half revolution. Vorticity grows secularly with time by successive passages across the shocks. When vorticity achieves substantial amplitudes, it causes the shock fronts to wiggle and fragment into small clumps with high vorticity (see Figure 4(c)). The process of clump formation along the shocks in our models bears remarkable resemblance to the wiggle instability of spiral shocks found by Wada & Koda (2004) (see also Kim & Ostriker 2006). These clumps are carried radially inward and add to the nuclear ring, making the latter fairly inhomogeneous (Figures 4(d) and (e)).

The off-axis shocks shown in Figure 5 are not stationary largely because the bar potential is not yet fully turned on. As the strength of the bar potential keeps increasing, they become stronger and move slowly toward the bar major axis. Gas that is added to the ring from the off-axis shocks has increasingly lower angular momentum with time, causing the ring to shrink in radius with time. After the bar potential is fully turned on, the off-axis shocks become gradually weaker as the amount of gas in the mid-bar regions lost to the ring increases with time. At the same time, orbital phase mixing and frequent clump collisions in the ring make the latter rounder and align its semimajor axis in the direction perpendicular to the bar major axis. Note that the rings are always attached to the inner end of the off-axis shocks.

At $t = 300$ Myr, Model cs05bh0 reaches a quasi-steady state in the sense that temporal changes in the overall flow pattern are very slow, and the locations of the shocks and rings do not vary much with time. Figure 4(f) overplots some of the x_1-orbits (dotted curves aligned vertically) and x_2-orbits (solid curves aligned horizontally), showing that the shape of the nuclear ring matches well with an x_2-orbit, while the off-axis shocks closely follow one of the x_1-orbits over the whole length of the shocks. This is because when $c_s = 5$ km s^{-1} the impact of thermal pressure on the gas orbits is much smaller than that of the gravitational and centrifugal forces, so that pure orbit theory (neglecting pressure forces) is a good description. When $c_s \gtrsim 15$ km s^{-1}, however, thermal pressure gradients strongly affect gas orbits, and thus the morphology of substructures in the central regions is modified, as we will discuss below.

3.2. Off-axis Shocks

Even if the gravitational potential is the same, the flow morphology and velocity fields differ considerably depending on the sound speed. Figure 7 shows instantaneous streamlines plotted over the logarithm of the density distribution in Models cs05bh0 and cs20bh0 at $t = 300$ Myr. Red curves denote the streamlines that go through the off-axis shocks, while those enveloping the off-axis shocks are represented by green curves. In all models, the off-axis shocks are almost parallel to x_1-orbits. They start from the bar major axis at the outer ends, offset toward downstream in the mid-bar regions, and connect to the nuclear rings at the inner ends. The mean offset of off-axis shocks from the bar major axis is larger for models with smaller c_s.

The outer end regions of the off-axis shocks have complicated density structures including the "4/1-spiral shocks" marked with a red arrow in Figure 7(a) (Englmaier & Gerhard 1997) and the enhanced density ridges (a white arrow) termed "smudges" by Patsis & Athanassoula (2000). As discussed by Englmaier & Gerhard (1997), the 4/1-spiral shocks are produced by collisions of gas moving on x_1-orbits with that on the 4/1-resonant family (e.g., Contopoulos & Grosbøl 1989). The gas loses angular momentum at the shocks and subsequently switches to lower
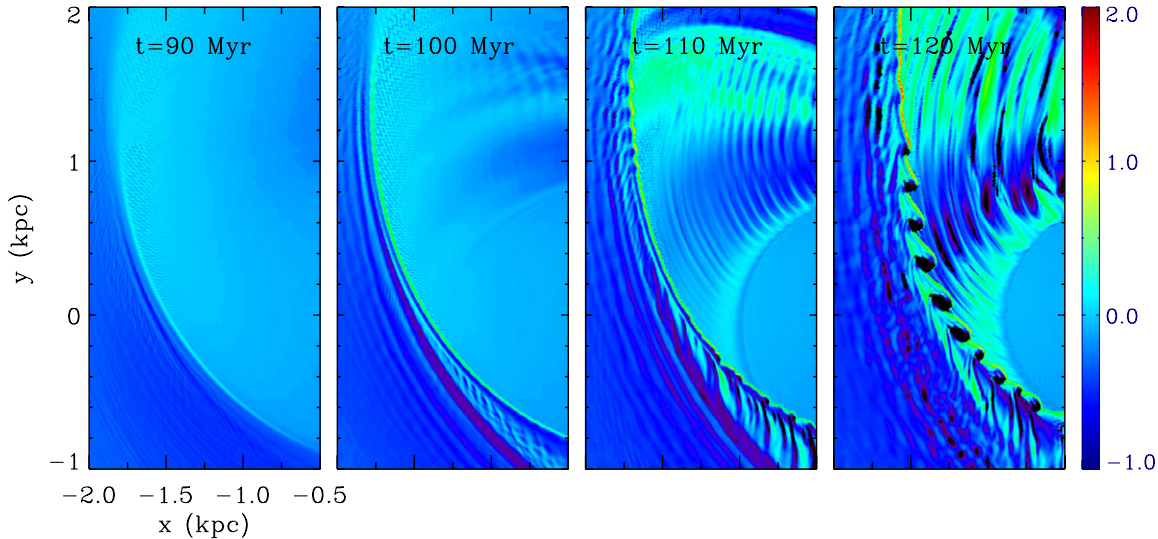
Figure 6. Snapshots of the potential vorticity $\xi \equiv |\nabla \times \mathbf{u} + 2\mathbf{\Omega}|/\Sigma$ normalized by the initial value ξ_0 in Model cs05bh0. Only the regions with -2 kpc $\leqslant x \leqslant -0.5$ kpc and -1 kpc $\leqslant y \leqslant 2$ kpc around the off-axis shocks are shown. The color bar shows $\log(\xi/\xi_0)$. This vortex-generating instability of curved shocks appears to be similar to the wiggle instability of spiral shocks identified by Wada & Koda (2004).

(A color version of this figure is available in the online journal.)
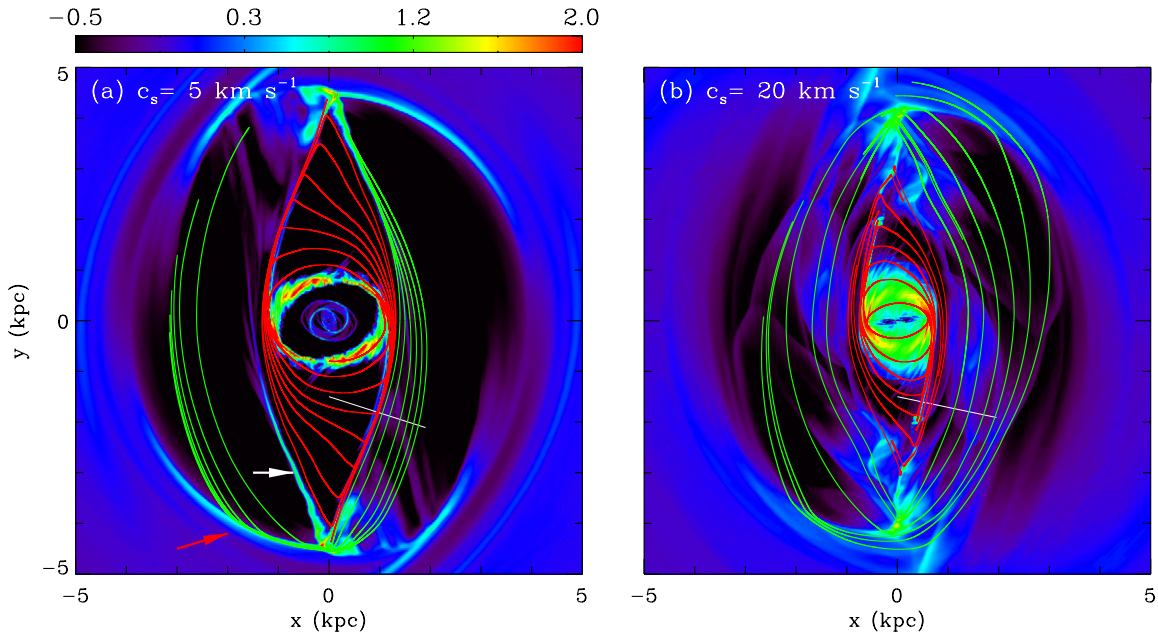
Figure 7. Logarithm of the density distribution overlaid with instantaneous streamlines in Models cs05bh0 and cs20bh0 at $t = 300$ Myr. The red lines represent streamlines that meet the off-axis shocks, while the green lines are for those that go around the shocks. The red and white arrows in (a) mark the 4/1-spiral shocks and "smudges," respectively. The short white line segment in each panel indicates a slit along which density and velocity are measured in Figure 8.

(A color version of this figure is available in the online journal.)

orbits. As the streamlines in green display, in models with $c_s = 5$ km s^{-1}, the 4/1-spiral shocks are quite strong and spatially extended, so that the orbits after the shocks become relatively radial and converge at the opposite side of the bar, building a smudge after about a half revolution. Collisions of streams off the 4/1-spiral shock and the smudge on the same side of the bar funnel the gas at the intersections to an x_1-orbit, which are the starting points of the off-axis shocks. When $c_s = 20$ km s^{-1}, on the other hand, the 4/1-spiral shocks are short and weak, and the streamlines off the shocks diverge, so that a dense ridge does not form. Since the gas becomes less compressible with increasing c_s, steady off-axis shocks in models with large c_s can be supported only in inner regions where the bar perturbations are sufficiently strong. This

explains why the mean offset of the off-axis shocks from the bar major axis becomes smaller as c_s increases (e.g., Englmaier & Gerhard 1997). With weak 4/1-spiral shocks and no smudge, the gas in the bar-end regions in a model with $c_s = 20$ km s^{-1} is comparatively unsteady, sometimes generating small dense blobs that move inward along the off-axis shocks.

To quantify the shock properties, we place a slit in each model, indicated by the short white lines in Figure 7. The slit starts from $(x, y) = (0, -1.5$ kpc) and runs perpendicular to the local segment of the off-axis shocks, roughly at $R \sim 1.5$–1.8 kpc. Figure 8 plots the profiles along the slit of surface density, velocities, and the compression factor,

$$\alpha \equiv -(\nabla \cdot \mathbf{v})\Delta R/c_s, \qquad (3)$$

Table 2
Properties of Off-axis Shocks

Model	$s_{\rm sh}$ (kpc)	$\Sigma_{\rm max}/\Sigma_0$	$\mathcal{M}_\perp$	$\mathcal{M}_\parallel$	$i_{\rm sh}$ (deg)	$dv_\parallel/ds$ (10^3 km s^{-1} kpc^{-1})	$\alpha_{\rm max}$
cs05bh0	0.98	5.7	12.1	10.9	47.7	2.7	7.2
cs10bh0	0.72	3.6	6.0	4.9	50.8	1.8	3.5
cs15bh0	0.55	5.7	5.7	1.0	80.4	2.3	2.6
cs20bh0	0.45	5.0	3.5	1.2	71.3	1.8	1.6
cs05bh7	0.93	5.8	15.4	6.3	67.9	1.8	7.4
cs10bh7	0.63	9.8	8.1	−1.3	−81.4	1.6	4.7
cs15bh7	0.47	9.0	6.6	−1.2	−79.8	1.7	3.0
cs20bh7	0.31	5.7	2.3	1.3	59.4	1.0	1.9
cs05bh8	0.96	6.1	16.7	7.2	66.7	2.0	7.5
cs10bh8	0.74	7.4	9.6	−0.1	−89.5	2.3	6.3
cs15bh8	0.43	6.8	7.2	−0.8	−83.3	1.4	3.0
cs20bh8	0.32	21.6	5.9	−2.6	−66.6	1.4	2.9

Notes. $s_{\rm sh}$ is the shock position along the slit; $\Sigma_{\rm max}$ is the maximum density attained immediately after $s_{\rm sh}$; $\mathcal{M}_\perp$ and $\mathcal{M}_\parallel$ are the Mach numbers of the incident flow perpendicular and parallel to the shock, respectively; $i_{\rm sh}$ is the inclination angle of the incident flow relative to the shock; $dv_\parallel/ds$ is the velocity shear in the post-shock region; $\alpha_{\rm max}$ is the maximum value (occurring at the shock front) of the compression factor $\alpha \equiv -(\nabla \cdot \mathbf{v})\Delta R/c_s$.
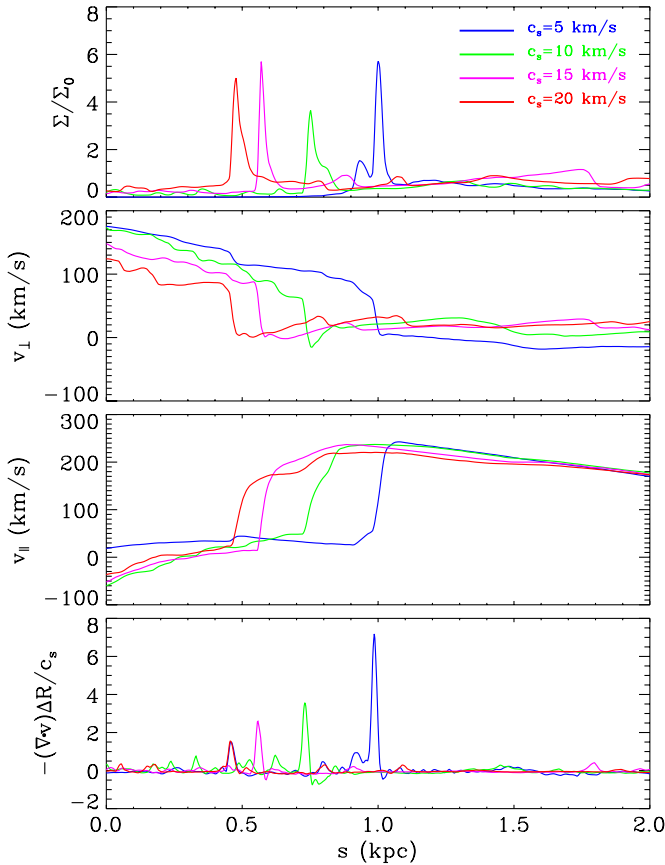
Figure 8. Profiles of surface density Σ, velocity $v_\perp$ perpendicular, and $v_\parallel$ parallel to the off-axis shock, and compression factor $\alpha = -(\nabla \cdot \mathbf{v})\Delta R/c_s$ along the slit in bh0 models with differing c_s at $t = 300$ Myr. The position of the slit is shown in Figure 7.

(A color version of this figure is available in the online journal.)

the last of which can be used as an effective measure of the shock strength (e.g., Maciejewski 2004b; Thakur et al. 2009).[10]

The gas is flowing from left to right in the increasing direction of s, where s measures the distance along the slit from the starting point. Table 2 gives the shock properties for all models at $t = 300$ Myr: $s_{\rm sh}$ is the position of the off-axis shocks along the slit, $\Sigma_{\rm max}$ is the peak density after $s_{\rm sh}$, $\mathcal{M}_\perp \equiv v_\perp/c_s$ and $\mathcal{M}_\parallel \equiv v_\parallel/c_s$ are the Mach numbers of the incident flows in the directions perpendicular and parallel to the shocks, respectively, $i_{\rm sh} \equiv \tan^{-1}(\mathcal{M}_\perp/\mathcal{M}_\parallel)$ is the inclination angle of the pre-shock velocity relative to the shock front, $dv_\parallel/ds$ quantifies the velocity shear in the post-shock region, and $\alpha_{\rm max}$ is the maximum value of the compression factor occurring at the shock front. It is apparent that the off-axis shocks tend to move toward the bar major axis with increasing c_s, while there is no clear dependence of $s_{\rm sh}$ on the BH mass. The compression factor at the shock is insensitive to $M_{\rm BH}$ and scales roughly with c_s as $\alpha_{\rm max} \sim 7.7(c_s/5 \ {\rm km \ s^{-1}})^{0.92}$.

Naively, one would expect that the off-axis shocks become weaker as the sound speed increases, since the density jump in planer isothermal shocks is proportional to $\mathcal{M}_\perp^2$. However, this is not the case, as Figure 8 and Table 2 demonstrate. There are several reasons for this. First, it is the velocity component normal to the shock front $v_\perp$ that determines the shock jump conditions, and because the inclination angle of the streamlines which enter the shock varies with location and with c_s, $v_\perp$ varies in a complicated fashion. For example, Figure 8 shows that for off-axis shocks formed at $R \sim 1.5$–1.8 kpc, Model cs15bh0 with $c_s = 15$ km s^{-1} has the largest peak density as well as the largest $v_\perp = 85$ km s^{-1} and $i_{\rm sh} = 80°$. On the other hand, Model cs10bh0 has the smallest $v_\perp = 60$ km s^{-1} (with $i_{\rm sh} = 51°$) and thus the lowest density enhancement. Since the sound speed is lower, Model cs05bh0 with $v_\perp = 60$ km s^{-1} produces $\Sigma_{\rm max}$ comparable to that in Model cs15bh0. Second, we note that the Rankine–Hugoniot jump conditions for stationary planar shocks are not applicable to the curved and two-dimensional off-axis shocks formed in our simulations. As Figure 7 displays, the flows are fully two dimensional in the sense that streamlines diverge before the shocks and converge after the shock with the radial inflow coming from the regions near the end of the bar. The fact that the compression factor α measured at the shock front is smaller than $\mathcal{M}_\perp - \mathcal{M}_\perp^{-1}$ expected from planer isothermal shocks also indicates that the shocks are two dimensional.

---

[10] For planar isothermal shocks in steady state, $\alpha = \mathcal{M}_\perp - \mathcal{M}_\perp^{-1}$ at the shock discontinuities.
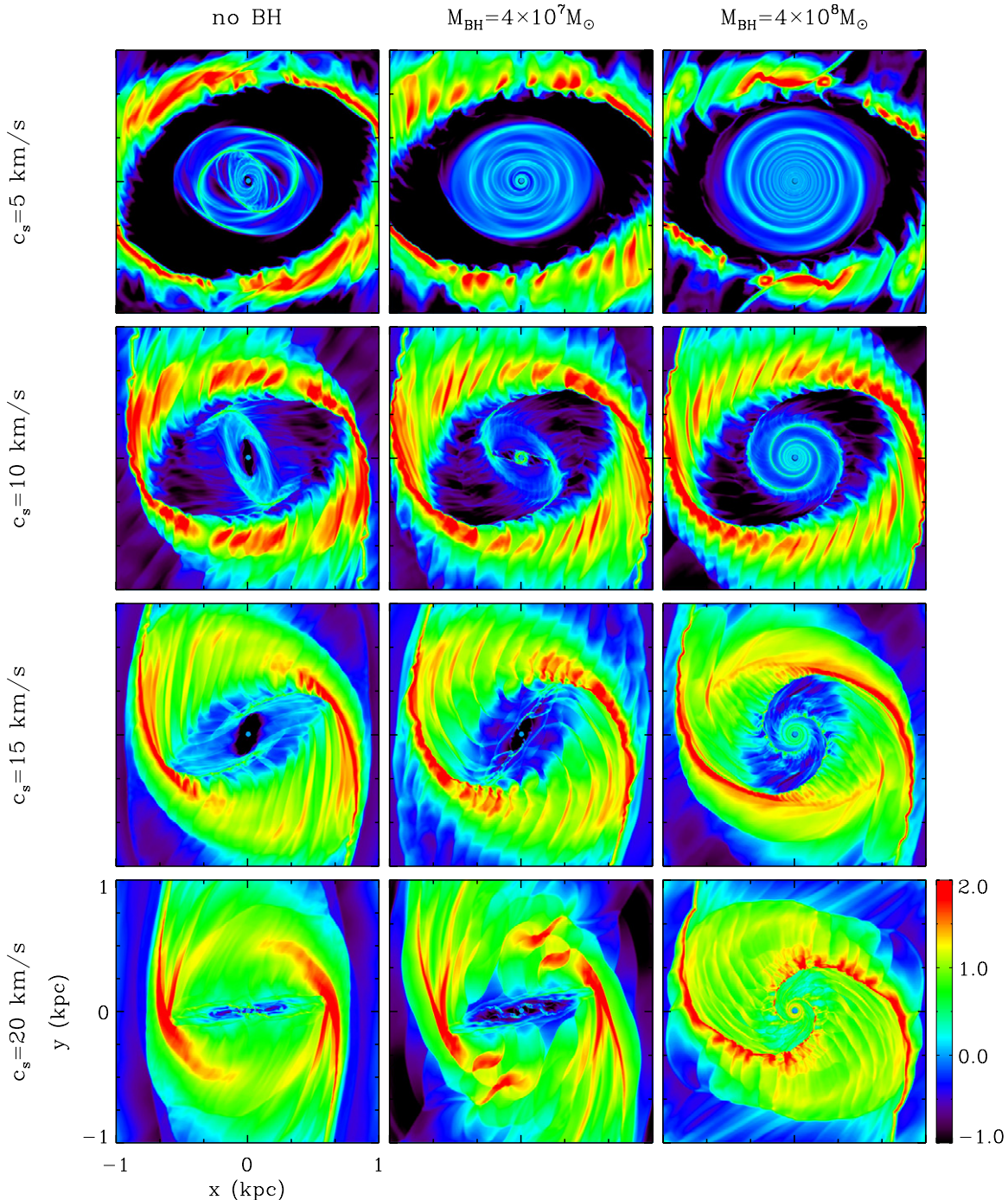
Figure 9. Effects of sound speed and BH mass on the distribution of gas surface density, shown in logarithmic scale, in the central regions of all models at $t = 300$ Myr. The nuclear rings are narrow when $c_s = 5$ km s^{-1}, while they spread out as c_s increases.

(A color version of this figure is available in the online journal.)

Finally, the density and velocity fluctuations generated by the vortex-generating instability are important around the off-axis shocks especially for models with small c_s, so that the flows are not strictly stationary.[11] Note that the shocked gas has strong velocity shear, amounting to $dv_\parallel/ds \sim (1\text{--}3) \times 10^3$ km s^{-1} kpc^{-1}, which is about 10 times larger than the velocity shear arising from galaxy rotation in the solar neighborhood. Such strong

shear can stabilize the high-density, off-axis shocks against self-gravity.

3.3. Nuclear Rings

Gas that loses angular momentum at the off-axis shocks flows radially inward and forms a nuclear ring in the central regions. Figure 9 shows diverse morphological features produced in the regions with $|x|, |y| \leqslant 1$ kpc for all models at $t = 300$ Myr. Figure 10 overplots instantaneous streamlines for a few selected models. Some models (with low c_s) have a nuclear ring together

---

[11] Negative values of $v_\perp$ right after the shocks in Model cs10bh0 shown in Figure 8 are due to vortices produced by the instability.
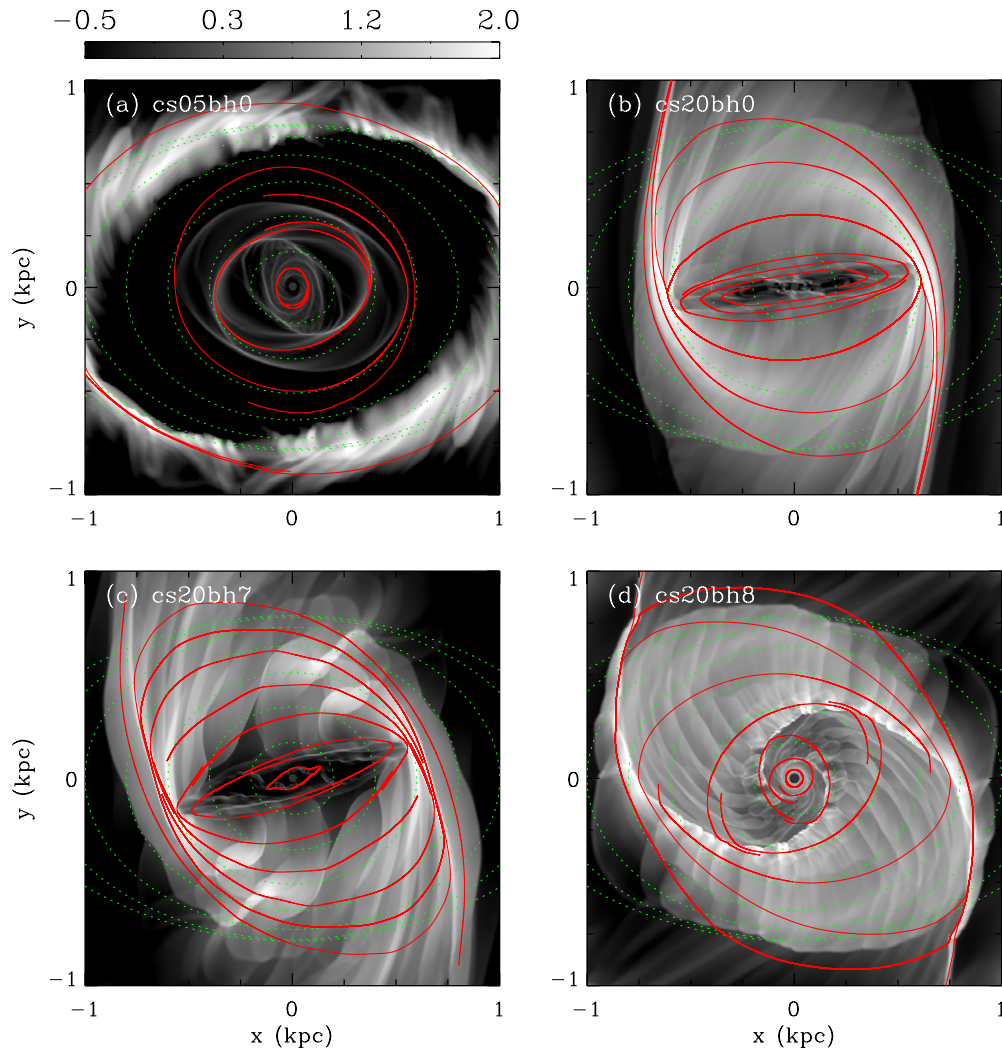
Figure 10. Instantaneous streamlines (red solid lines) overlaid on the logarithm of the density distribution for models with (a) $c_s = 5$ km s^{-1} and no BH, (b) $c_s = 20$ km s^{-1} and no BH, (c) $c_s = 20$ km s^{-1} and $M_{\rm BH} = 4 \times 10^7 \ M_{\odot}$, and (d) $c_s = 20$ km s^{-1} and $M_{\rm BH} = 4 \times 10^8 \ M_{\odot}$, at $t = 300$ Myr. The dotted curves in all panels represent x_2-orbits.

(A color version of this figure is available in the online journal.)

with inner spiral structures, some models (with high c_s and small $M_{\rm BH}$) have a ring with no apparent spirals, while others (with high c_s and large $M_{\rm BH}$) possess only nuclear spirals without an appreciable ring.

When $c_s = 5$ km s^{-1}, the nuclear rings are quite narrow and clearly decoupled from the nuclear spirals. Even though the ring has a large density, the low sound speed makes the effect of thermal pressure on the gas orbits insignificant. The gas around the ring in Model cs05bh0 thus follows x_2-orbits fairly well and the shape of the ring does not deviate considerably from x_2-orbits (Figure 10(a)). When $c_s = 20$ km s^{-1}, on the other hand, the pressure force in the central regions becomes important and affects the shape of the gas streamlines. Even the inflowing gas that arrives at the contact points between the off-axis shocks and the nuclear ring takes very different orbits depending on its location. Some gas at the outer parts of the contact points is pushed out by the pressure gradient and follows trajectories that are much rounder than x_2-orbits, while the gas in the inner parts is forced to take inner highly eccentric orbits (Figure 10(b)). Consequently, the gas in the central regions in Models cs20bh0 spreads out spatially and forms a ring that is more circular and broader than in Model cs05bh0. Since the presence of a central

BH increases the initial angular momentum of the gas in the central regions, the pressure effect becomes less important as $M_{\rm BH}$ increases. Figure 10 shows that the pressure distortion of x_2-orbits is still significant for $M_{\rm BH} = 4 \times 10^7 \ M_{\odot}$, while the gas orbits in the very central parts at $R \lesssim 0.2$ kpc remain almost intact when $M_{\rm BH} = 4 \times 10^8 \ M_{\odot}$. In Model cs20bh8, some gas at $R \sim 0.5$–0.8 kpc temporarily moves radially outward due to the radial pressure gradient built up by the background gas and is subsequently swept inward by other gas flowing in along the off-axis shocks.

Figure 11 plots the radial distribution of the averaged gas surface density $\langle \Sigma \rangle$, averaged both azimuthally and temporally over $t = 300$–500 Myr for all models. The locations of the ILRs as well as $R_{\rm max}$ and $R_{\rm min}$ corresponding to the local maximum and minimum of the $\Omega - \kappa/2$ curve are indicated by arrows on the abscissa. Table 3 gives the inner and outer radii, $R_{\rm in}$ and $R_{\rm out}$, of the ring, the mass-weighted ring radius $R_{\rm ring} = \int_{R_{\rm in}}^{R_{\rm out}} \langle \Sigma \rangle R \, dR / \int_{R_{\rm in}}^{R_{\rm out}} \langle \Sigma \rangle \, dR$, the peak density $\langle \Sigma \rangle_{\rm max}$, and the mean density $\Sigma_{\rm ring} = \int_{R_{\rm in}}^{R_{\rm out}} \langle \Sigma \rangle \, dR / (R_{\rm out} - R_{\rm in})$ of the ring in each model. Here, $R_{\rm in}$ and $R_{\rm out}$ are defined as the radii where $\langle \Sigma \rangle = \langle \Sigma \rangle_{\rm max}/5$. Note that Models cs15bh8 and cs20bh8 do not
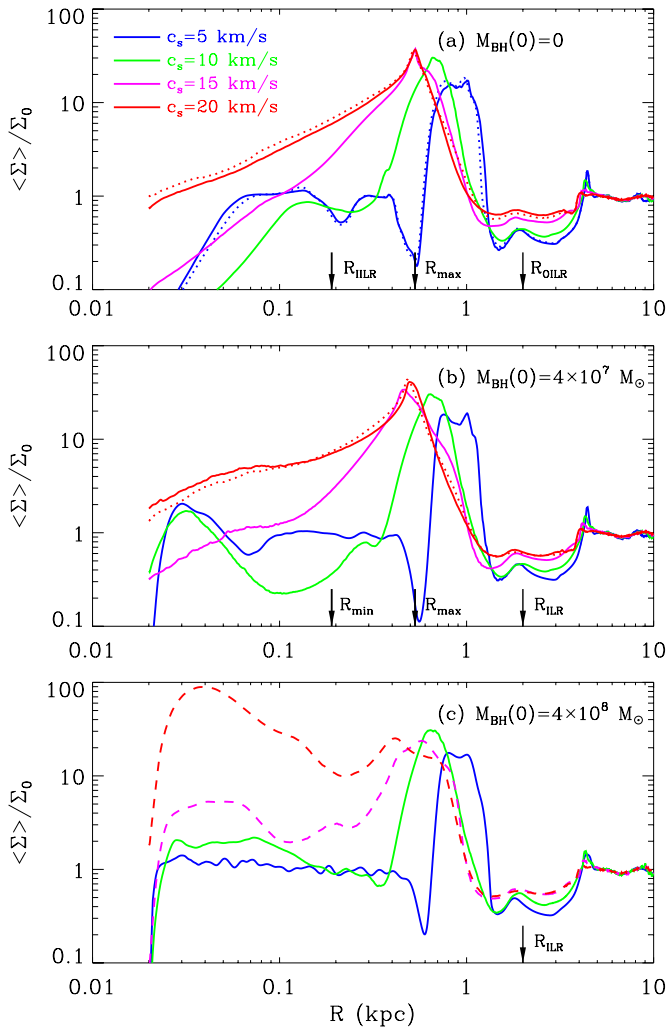
Figure 11. Radial distribution of gas surface density $\langle\Sigma\rangle$ averaged both azimuthally and temporally over $t = 300$–500 Myr for models with (a) $M_{\rm BH}(0) = 0$, (b) $M_{\rm BH}(0) = 4 \times 10^7\ M_\odot$, and (c) $M_{\rm BH}(0) = 8 \times 10^7\ M_\odot$. The dotted lines are the results of the models in which $M_{\rm BH}$ varies with time. The locations of $R_{\rm max}$ and $R_{\rm min}$ where the $\Omega - \kappa/2$ curve attains local maximum and minimum and the relevant ILRs are indicated as arrows along the abscissa. In (c), the dashed lines correspond to the cases with $c_s = 15$ or 20 km s^{-1} for which the density at $R < 0.1$ kpc is dominated by nuclear spirals rather than rings.

(A color version of this figure is available in the online journal.)

harbor a well-defined nuclear ring, as will be discussed in the next section.

All rings that form are located within $R_{\rm OILR}$ if there are two ILRs or $R_{\rm ILR}$ if there is a single ILR, indicating that the formation of a nuclear ring does not require the presence of two ILRs. However, there is in general no direct connection between the ring positions and $R_{\rm OILR}$ or $R_{\rm ILR}$. When $c_s = 5$ km s^{-1}, the rings are all located at $R \sim 0.6$–1.2 kpc, independent of $M_{\rm BH}$. The mass-weighted radius is $R_{\rm ring} \sim 0.90$–0.92 kpc, indicating that the ring position is not governed by the shape of the $\Omega - \kappa/2$ curve. When $c_s = 10$ km s^{-1}, the ring radius decreases to $R_{\rm ring} \sim 0.67$–0.68 kpc, again insensitive to the BH mass, consistent with the tendency for the off-axis shocks to move closer to the bar major axis as c_s increases. Rings with $c_s = 10$ km s^{-1} have a larger surface density than those with $c_s = 5$ km s^{-1}, corresponding approximately to a constant ring mass (i.e., $\Sigma_{\rm ring} \propto R_{\rm ring}^{-1}$). As c_s increases further, high thermal pressure provides strong perturbations for x_2-orbits and

Table 3
Properties of Nuclear Rings

Model	$R_{\rm in}$ (kpc)	$R_{\rm out}$ (kpc)	$R_{\rm ring}$ (kpc)	$\langle\Sigma\rangle_{\rm max}/\Sigma_0$	$\Sigma_{\rm ring}/\Sigma_0$
cs05bh0	0.63	1.22	0.92	17.2	11.9
cs05bh0t	0.62	1.17	0.89	18.4	13.1
cs10bh0	0.45	0.90	0.68	30.2	17.9
cs15bh0	0.30	0.77	0.54	37.5	17.6
cs20bh0	0.23	0.71	0.49	36.8	16.9
cs20bh0t	0.20	0.73	0.48	34.7	16.1
cs05bh7	0.66	1.17	0.90	18.9	13.9
cs10bh7	0.46	0.88	0.67	30.3	18.9
cs15bh7	0.28	0.80	0.52	33.9	16.9
cs20bh7	0.23	0.67	0.47	41.0	19.5
cs20bh7t	0.22	0.66	0.46	43.4	19.9
cs05bh8	0.69	1.25	0.94	18.1	12.7
cs10bh8	0.47	0.89	0.67	30.9	19.4
cs15bh8	...	...	...	...	...
cs20bh8	...	...	...	...	...

Notes. $R_{\rm in}$ and $R_{\rm out}$ are the inner and outer radii of the ring defined by the positions where $\langle\Sigma\rangle = \langle\Sigma\rangle_{\rm max}/5$, with $\langle\Sigma\rangle_{\rm max}$ being the maximum density; $R_{\rm ring}$ is the mass-weighted ring radius; $\Sigma_{\rm ring}$ is the mean density of the ring.

tends to spread out the gas in the central parts, resulting in a broad distribution of $\langle\Sigma\rangle$ at $R \lesssim 0.5$ kpc. When the BH is not massive enough, these perturbations wipe out coherent, weak spiral structures that formed earlier in the nuclear regions.

Because the presence of a central BH dominates the potential only in the central region, the allowance for the growth of the BH due to mass accretion does not make a significant difference in the regions outside the ring. Even inside the ring, Figure 11 and Table 3 show that the changes in the ring size $R_{\rm ring}$ and the ring density $\Sigma_{\rm ring}$ caused by the temporal change of $M_{\rm BH}$ are less than 4% and 10%, respectively. We will show below that BH growth in our simulations also does not significantly affect the properties of nuclear spirals and mass inflow rates.

4. NUCLEAR SPIRALS

High-resolution observations of barred galaxies reveal that some contain nuclear spirals inside a nuclear ring (e.g., Martini et al. 2003a, 2003b; Prieto et al. 2005; van de Ven & Fathi 2010). As Figure 9 shows, some of our models also have spiral structures in their nuclear regions that persist for long periods of time. Other models also have nuclear spirals at early time but they are destroyed as a result of interactions with nuclear rings. In this section, we describe the formation and shape of nuclear spirals in detail. Figure 12 schematically summarizes how the type of nuclear spirals changes with time and how long they survive in each model. Table 4 lists the properties of nuclear spirals measured at $t = 500$ Myr for the models that possess long-lasting spirals: $R_{\rm in}$ and $R_{\rm out}$ denote the radii of the inner and outer ends of the nuclear spirals, respectively; $\Sigma_{\rm avg}$ and $\Sigma_{\rm peak}$ are the azimuthally averaged and peak surface densities, respectively, at $R = R_a = 0.05$ kpc for Models cs15bh8 and cs20bh8 and $R_a = \sqrt{R_{\rm in} R_{\rm out}}$ for the other models; i_p is the pitch angle of the spirals at $R = R_a$. A negative (positive) value of i_p indicates leading (trailing) spirals.

4.1. Models without a Black Hole

To study the spiral features, it is convenient to show the logarithm of the gas surface density in logarithmic polar
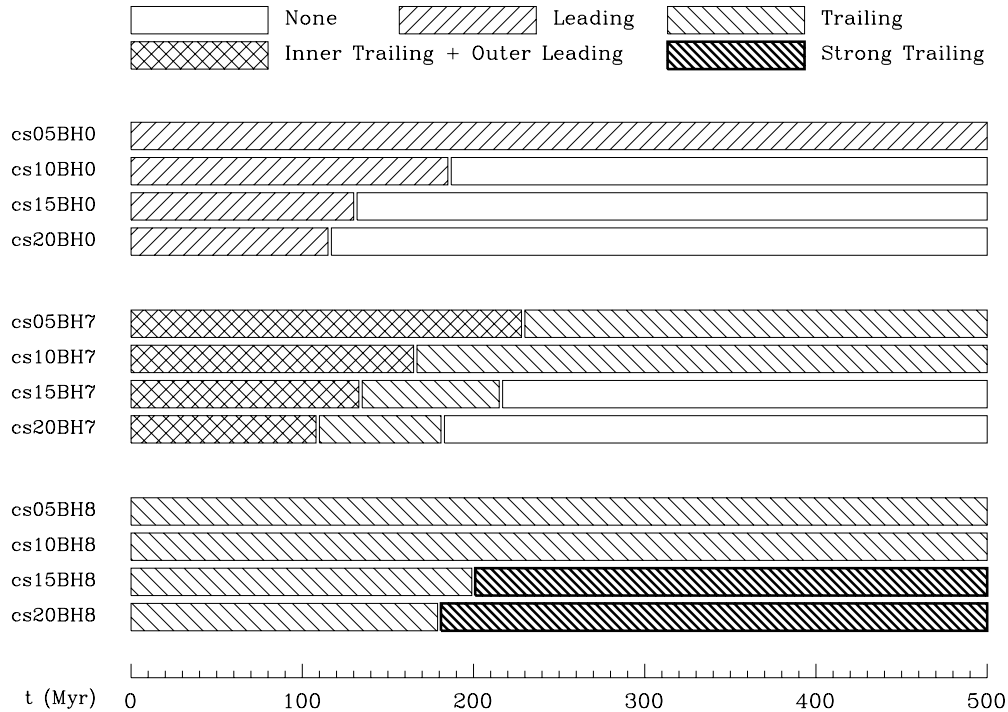
Figure 12. Schematic illustration of the types of nuclear spirals found in our simulations, and their duration.

Table 4
Properties of Nuclear Spirals

Model	$R_{\rm in}$ (kpc)	$R_{\rm out}$ (kpc)	$\Sigma_{\rm avg}/\Sigma_0$	$\Sigma_{\rm peak}/\Sigma_{\rm avg}$	i_p (deg)
cs05bh0	0.13	0.50	0.41	7.92	−33.8
cs05bh0t	0.20	0.45	0.56	9.84	−35.4
cs05bh7	0.02	0.45	0.92	1.95	8.5
cs10bh7	0.05	0.42	0.16	3.86	55.1
cs05bh8	0.02	0.55	1.00	2.07	3.5
cs10bh8	0.02	0.40	2.28	1.91	5.8
cs15bh8	0.02	. . .	8.09	1.67	6.2
cs20bh8	0.02	. . .	170.0	1.74	7.8

Notes. $R_{\rm in}$ and $R_{\rm out}$ are the inner and outer ends; $\Sigma_{\rm avg}$ and $\Sigma_{\rm peak}$ are the mean and peak densities at $R_a = 0.05$ kpc for Models cs15bh8 and cs20bh8 and $R_a = (R_{\rm in} R_{\rm out})^{1/2}$ for the other models; i_p is the pitch angle at $R = R_a$.

coordinates. Figure 13 plots snapshots of gas surface density of Models cs05bh0 and cs10bh0 on the $\phi - \log R$ plane. Any coherent features with a positive (negative) slope on this plane are leading (trailing) waves. Only the regions with $R \leqslant 1$ kpc are shown. Two horizontal lines mark $R_{\rm IILR}$ and $R_{\rm max}$ where the $\Omega - \kappa/2$ curve is a locally maximum. At early time, the non-axisymmetric bar potential induces weak $m = 2$ perturbations in the central regions. Perturbed gas elements in the galactic plane follow slightly elliptical orbits, which are closed in a frame rotating at $\Omega - \kappa/2$ and thus precess at a rate $\Omega - \kappa/2$ near the ILRs when seen in a stationary bar frame. As succinctly depicted in Buta & Combes (1996), due to collisional dissipation of gas kinetic energy occurring on converging orbits, the gas forms spiral structures whose shape depends critically on the sign of $d(\Omega - \kappa/2)/dR$ such that spirals are leading (trailing) where $d(\Omega - \kappa/2)/dR$ is positive (negative). Figure 13 indeed shows that when $t = 50$ Myr the perturbed density is leading at $R < R_{\rm max}$ and trailing at $R > R_{\rm max}$, although the trailing

features are soon overwhelmed by the nuclear ring. Located away from the nuclear ring, however, the inner leading waves are able to grow with time and eventually develop into shock waves at $t \sim 200$ Myr. These nuclear spirals are short, extending over $R \sim 0.13$–0.50 kpc, quite open with a pitch angle of $i_p = -30°$, and almost completely detached from the nuclear ring.

Figure 14 plots the azimuthal distributions of surface density and velocities of the nuclear spirals at $R = 0.25$ kpc in Models cs05bh0 (solid lines) and cs05bh0t (dotted lines) when $t = 500$ Myr. Over the course of the orbits, the changes of the radial and azimuthal velocities associated with the spirals amount to $\sim$100 km s^{-1}, which is indeed large enough to induce shocks. The peak densities occurring at $\phi \sim 100°, 280°$ for Model cs05bh0 correspond to shock fronts with a compression factor of $\alpha \sim 3.4$. The density bumps at $\phi \sim 135°, 315°$ are produced by waves launched from the inner boundary. In Model cs05bh0t, the BH mass is increased to $M_{\rm BH} \sim 10^5\,M_\odot$ due to mass inflow, which supports slightly stronger, more leading spiral shocks than in Model cs05bh0 with no BH. Despite continual perturbations by traveling trailing waves propagating from the inner boundary, the nuclear spirals in these models last until the end of the run. That leading nuclear spirals are persistent when the sound speed is small is consistent with the results of SPH simulations reported by Ann & Thakur (2005).
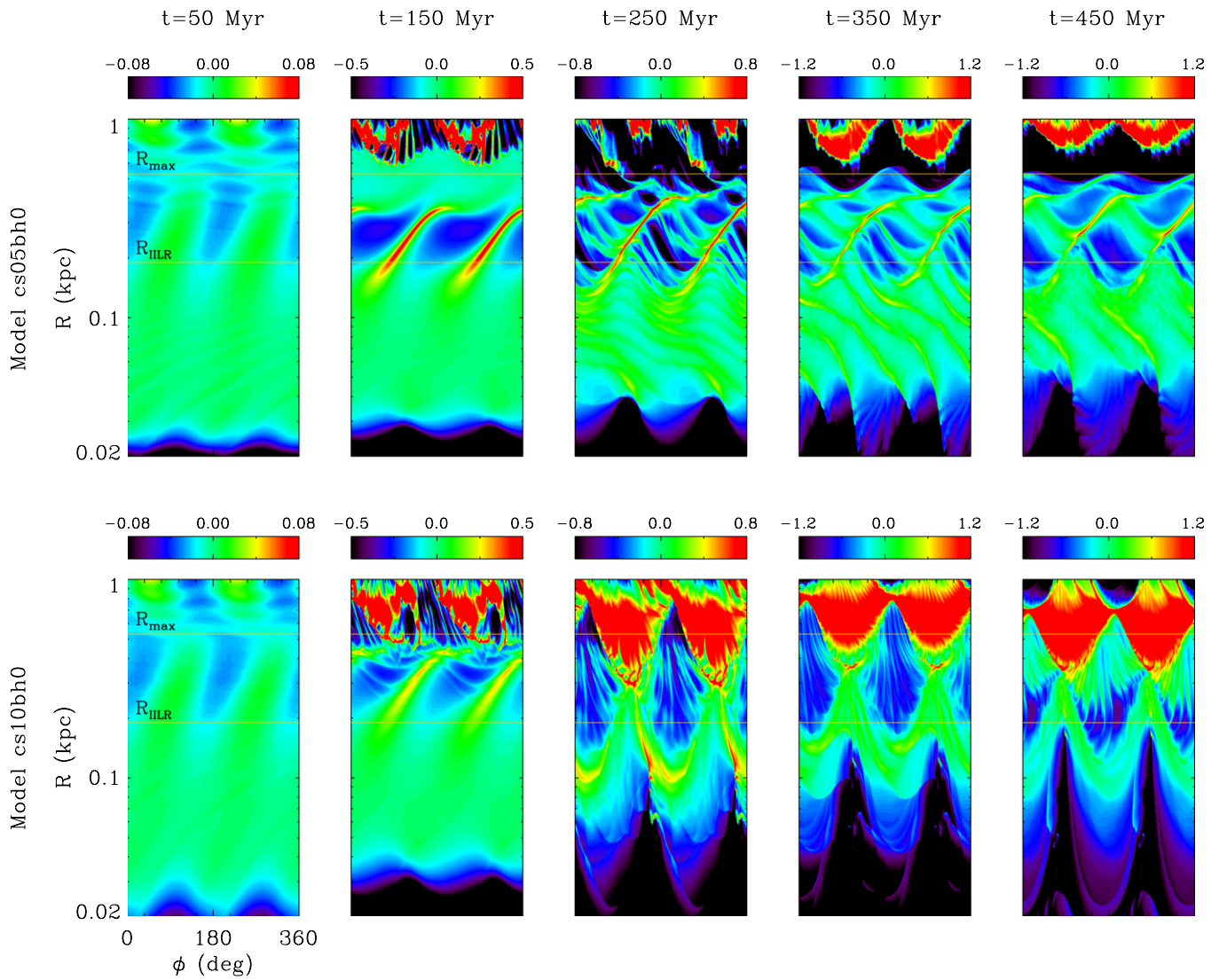
The usual WKB dispersion relation for tightly wound, linear-amplitude waves in a non-self-gravitating medium reads

$$(\omega - m\Omega)^2 = k^2 c_s^2 + \kappa^2, \qquad (4)$$

where ω is the wave frequency and k and m are the radial and azimuthal wavenumbers (e.g., Goldreich & Tremaine 1978). For $m = 2$ waves corotating with a bar (i.e., $\omega = 2\Omega_b$), Equation (4) becomes

$$k = \pm \frac{2}{c_s}\sqrt{(\Omega + \kappa/2 - \Omega_b)(\Omega - \kappa/2 - \Omega_b)}, \qquad (5)$$

Figure 13. Snapshots of the logarithm of the gas surface density on the $\phi - \log R$ plane for Models cs05bh0 (top row) and cs10bh0 (bottom row). These models do not have a central BH. Only the regions with $R \leqslant 1$ kpc are shown. The locations of R_{IILR} and R_{max} are indicated by two horizontal lines.

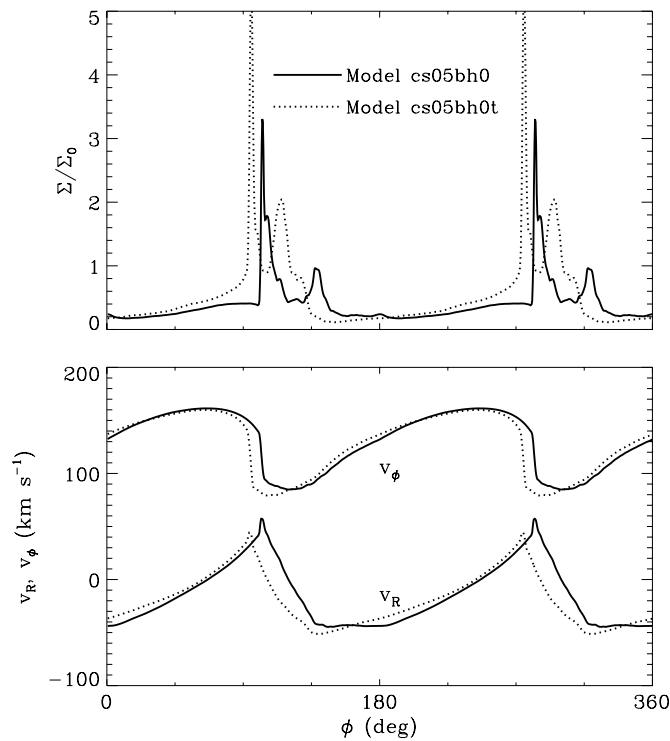(A color version of this figure is available in the online journal.)

(e.g., Englmaier & Shlosman 2000; Maciejewski 2004a), indicating that nuclear spirals corotating with the bar can exist only in the regions between R_{IILR} and R_{OILR} when there are two ILRs.[12] However, the top row in Figure 13 reveals that the nuclear spirals in Model cs05bh0 extend slightly inward of R_{IILR}. This seemingly contradicting result is due to nonlinear effects which are not captured by the WKB theory. The velocity perturbations associated with these spirals are so large that fluid elements just outside R_{IILR} can move across the inner ILR over the course of their epicycle orbits, providing perturbations for the gas at $R < R_{\mathrm{IILR}}$ that responds passively. In Model cs05bh0, the radial velocity perturbation is $\Delta v_R = 52$ km s^{-1}. Since the epicycle frequency is $\kappa = 1100$ km s^{-1} kpc^{-1} at $R = R_{\mathrm{IILR}}$, the corresponding radial amplitude of the epicycle orbits is estimated to be $\Delta R = \Delta v_R / \kappa = 0.05$ kpc, which is in good agreement with the radial extent of the nuclear spirals inward of R_{IILR}.

Models without a BH and with $c_s \geqslant 10$ km s^{-1} do form nuclear spirals at early time, but they are all transient, lasting less than 200 Myr. The bottom row of Figure 9 shows how nuclear spirals are destroyed in Model cs10bh0. The nuclear ring in this model is not only located inside R_{max} but also has large thermal pressure, continuously generating sonic perturbations that propagate radially inward. Because of the background shear, the perturbations are preferentially in the form of trailing waves which interact destructively with the leading spirals that formed at $R < R_{\mathrm{max}}$, destroying the latter. The destruction of nuclear spirals happens at $t = 185$ Myr for Model cs10bh0. This occurs earlier as c_s increases, since disturbing pressure perturbations are correspondingly stronger.

4.2. Models with $M_{\mathrm{BH}} = 4 \times 10^7 \, M_{\odot}$

Since the presence of a central BH greatly changes the $\Omega - \kappa/2$ curve in the central regions, it is interesting to explore how the morphologies of nuclear spirals depend on the BH mass. In bh7 and bh8 models with a single ILR, stationary waves in the bar frame can exist inside R_{ILR} all the way down to the center. Figure 15 plots snapshots of gas surface density for Models

---

[12] Figure 13 shows that there are low-amplitude waves propagating relative to the bar inside R_{IILR}. Such waves can exist inside the inner ILR as long as they satisfy Equation (4) in the WKB limit.

Figure 14. Azimuthal profiles of surface density (top) and velocities (bottom) of the nuclear spirals at $R = 0.25$ kpc in Models cs05bh0 (solid) and cs05bh0t (dotted) when $t = 500$ Myr. The spirals at this radius are shocks with the compression factor of $\alpha \sim 3.4$.

cs05bh7 and cs10bh7 on the logarithmic polar plane. The positions of $R_{\max}$ and $R_{\min}$ are indicated by the horizontal lines. As expected, the overdense perturbations produced by orbit crowding at early time ($t = 50$ Myr) have leading configurations at $R_{\min} < R < R_{\max}$ and trailing configurations at $R < R_{\min}$ or $R > R_{\max}$. The overdense regions at $R > R_{\max}$ are subsequently wiped out as the nuclear ring forms, while those at $R < R_{\max}$ grow into trailing nuclear spirals. In Model cs05bh7, the leading spirals at $R_{\min} < R < R_{\max}$ also grow slightly until $t \sim 150$ Myr to temporarily form "inner-trailing and outer-leading" structures represented by the double cross-hatching in Figure 12. As trailing perturbations from both the inner trailing spirals and the outer nuclear ring propagate and interfere with the leading spirals, it becomes increasingly difficult to identify coherent spiral structures at $R_{\min} < R < R_{\max}$. On the other hand, the trailing spirals at $R < R_{\min}$ keep growing until $t \sim 230$ Myr after which their amplitude of $\Sigma_{\mathrm{peak}}/\Sigma_{\mathrm{avg}} \approx 2.0$ remains more or less constant. They are approximately logarithmic in shape with a pitch angle of $i_p = 8.5$. Unlike in Model cs05bh0 where leading spirals are actually shocks, the trailing nuclear spirals in Models cs05bh7 are relatively weak (with the maximum compression factor of $\alpha_{\max} \sim 0.28$ at $t = 500$ Myr) and never develop into shocks.

In Model cs10bh7 (bottom row of Figure 15), the nuclear spirals have larger k and thus are more open than those in the $c_s = 5$ km s^{-1} counterparts (see, e.g., Equation (5)). Since the nuclear ring in this model forms at $R_{\mathrm{ring}} \approx 0.5$ kpc, it can directly destroy the leading spiral at $R_{\min} < R < R_{\max}$, and feeds the inner trailing spirals by supplying trailing perturbations. Thus, the inner spirals grow both in strength and spatial extent to make contact with the nuclear ring at $t = 210$ Myr. At this time, all parts of the nuclear spirals turn to shocks with the maximum density of $\Sigma_{\max}/\Sigma_0 = 3.8$ and the

corresponding compression factor of $\alpha = 0.8$ at $R = 0.1$ kpc. Gas passing through the spiral shocks loses angular momentum, increasing the mass inflow rate at the inner boundary. As the amount of gas lost in the nuclear regions increases, the density of the nuclear spirals decreases with time, but they remain as shocks with the compression factor of $\alpha \sim 1.3$ until the end of the run.

In Models cs15bh7 and cs20bh7, nuclear spirals start out with inner-trailing and outer-leading shapes, and evolve into trailing-only configurations, as in the other bh7 models. However, the highly eccentric orbits of the gas affected by thermal pressure dismantle the inner spiral structures almost completely in these models: thermal perturbations are so strong that a central BH with $M_{\mathrm{BH}} = 4 \times 10^7 \, M_\odot$ cannot enforce circular orbits in the very nuclear regions (see Figure 10(c)).

### 4.3. Models with $M_{\mathrm{BH}} = 4 \times 10^8 \, M_\odot$

Since the $\Omega - \kappa/2$ curve decreases monotonically with $R < 1$ kpc in bh8 models, nuclear spirals, if they exist, are all trailing as evident in Figure 16. For Model cs05bh8 (top row of Figure 16), the spirals evolve almost independently of, and are well separated from, the nuclear ring. At $t = 500$ Myr, they have a very small pitch angle $i_p = 3.5$ corresponding to $kR = 2 \cot i_p = 33$ owing to the strong background shear. They are also very weak, with an amplitude of $\Sigma_{\mathrm{peak}}/\Sigma_{\mathrm{avg}} = 2.1$ at $R \approx 0.1$ kpc. When $c_s = 10$ km s^{-1}, the pitch angle is increased to $i_p = 5.8$ and the nuclear spirals extend outward all the way to the nuclear ring. Except near the contact points, the spirals are still decoupled from the ring. With quite a large value of $kR = 20$, the component of the rotational velocity perpendicular to the spirals is not large enough to induce shocks.

We have seen earlier that the large thermal pressure in the rings of models with $c_s \geqslant 15$ km s^{-1} provides strong perturbations that make the gas orbits near the galaxy center highly eccentric, destroying nuclear spirals in bh0 and bh7 models. In bh8 models, however, the situation is quite different since a central BH with $M_{\mathrm{BH}} = 4 \times 10^8 \, M_\odot$ dominates the potential, keeping the orbits almost circular in the very central regions. Even with a large thermal pressure, the gas orbits there cannot be very eccentric, so that the nuclear spirals are protected from disruptive pressure perturbations. On the other hand, the ring material is quite distributed because of the large pressure gradients, feeding a trailing nuclear spiral that grows strongly in Models cs15bh8 and cs20bh8.

At $t = 120$ Myr, the spirals in Models cs15bh8 and cs20bh8 turn into shocks and touch the densest parts of the ring located at $R \sim 0.4$ kpc. Because of the larger pitch angles, the shocks are stronger in the outer parts; the portions at $R \lesssim 0.1$ kpc are weak shocks with density jumps of only ~ 2. Similarly, the shocks in Model cs20bh8 are stronger than those in Model cs15bh8 since the former has more open spirals and a denser ring. In both models, the shocks near the ring are so strong that even the gas constituting the ring suffers from a significant loss of angular momentum at the intersecting points. At $t = 150$ Myr, the ring material is essentially dissected by the trailing spiral shocks and gradually moves toward the center. As the ring material continues to flow in, the spirals appear as a direct continuation of the off-axis shocks ($t = 350$ Myr), consistent with the results of Maciejewski (2004b).

Figure 17 plots the radial distributions of the maximum and mean densities as well as the maximum compression factor in the inner 1 kpc regions of Models cs15bh8 and cs20bh8 at $t = 500$ Myr. The inflow of the ring material in Model
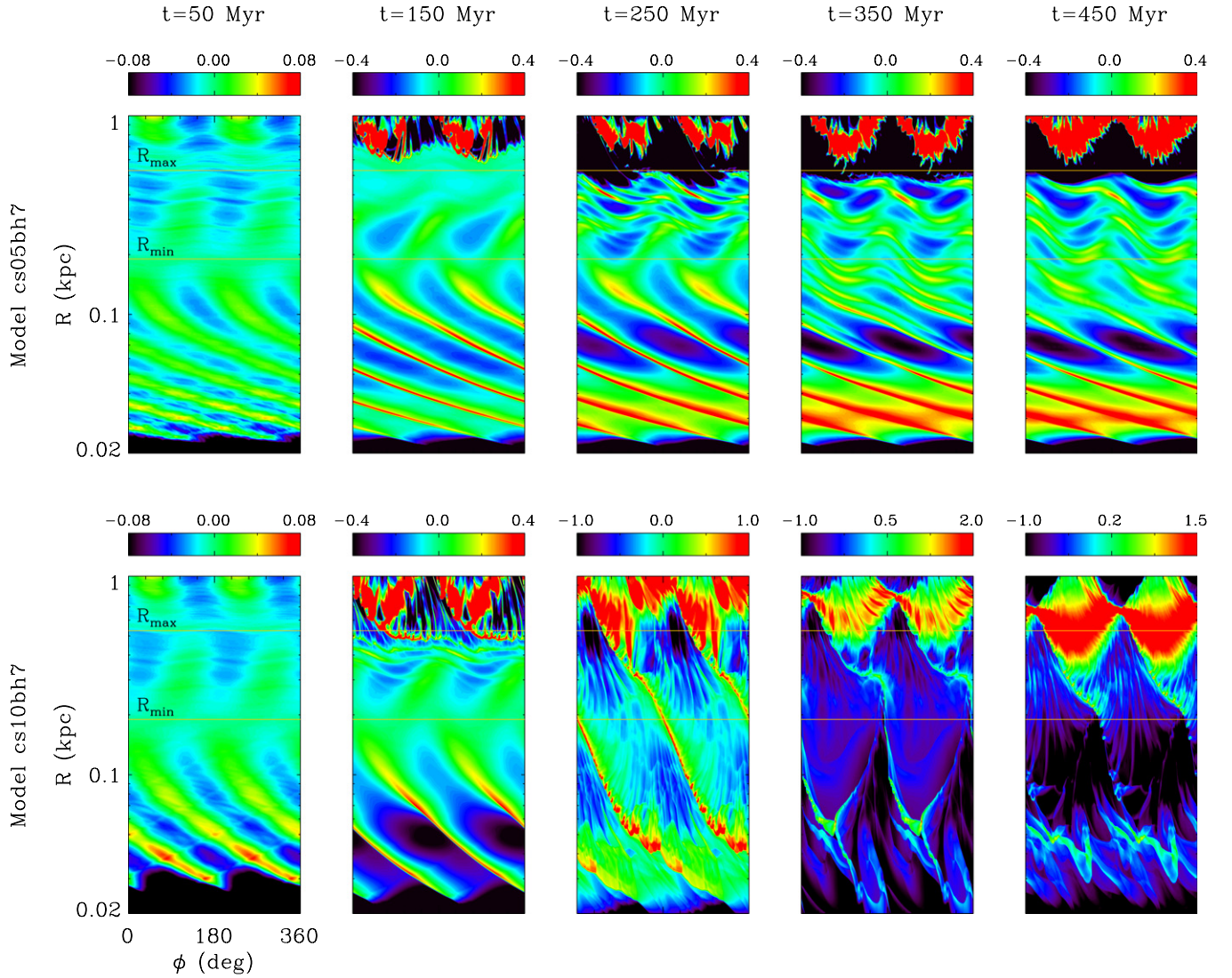
Figure 15. Snapshots of the logarithm of the gas surface density on the $\phi - \log R$ plane for Models cs05bh7 (top row) and cs10bh7 (bottom row). These models have a central BH with a mass of $4 \times 10^7 \, M_\odot$. Only the regions with $R \leqslant 1$ kpc are shown. The locations of $R_{\max}$ and $R_{\min}$ are indicated by two horizontal lines.
(A color version of this figure is available in the online journal.)

cs20bh8 is sufficiently strong that the gas is collected in the nuclear regions with $R \sim 0.02$–0.1 kpc; the amount of the gas that goes out through the inner boundary is much smaller than that which comes in. With weaker shocks and thus less angular momentum loss, on the other hand, the destroyed ring gas in Model cs15bh8 is still mostly at $R > 0.1$ kpc at this time. Note that the density enhancement at $R = 0.05$ kpc resulting from the dissolution of the ring is $\sim 8\Sigma_0$ and $\sim 170\Sigma_0$ in Models cs15bh8 and cs20bh8, respectively: the mean contrast of the spirals that are weak shocks with the compression factor $\alpha \sim 0.3$ is $\Sigma_{\mathrm{peak}}/\Sigma_{\mathrm{avg}} \sim 1.6$–$1.8$ at $R = 0.05$ kpc in both models. This increase of the gas surface density in the central regions is the primary reason for enhanced mass inflow rates at late time in bh8 models with large c_s.

5. MASS INFLOW RATES

Galactic bars are considered to be a promising means of transporting gas to the centers of galaxies to fuel supermassive BHs and produce AGNs. Since our numerical models use a cylindrical grid with a circular boundary, they are ideally suited

to study how the mass accretion rate depends on the gas sound speed and the BH mass. We assume that all the gas that crosses the inner boundary located at $R = 20$ pc in our models is accreted to the central BH. In reality, a large amount of mass in gas near the BH may change the gas orbits by providing pressure and gravitational forces. Therefore, $\dot{M}$ through the inner boundary that we measure is likely to be an upper limit to the real mass accretion rate to the BH. In addition, $\dot{M}$ is likely to depend on the inner boundary size especially when gas orbits are highly eccentric near the inner boundary. Note that in non-self-gravitating, isothermal, and unmagnetized systems, $\dot{M}$ resulting from simulations is linearly proportional to the adopted initial surface density Σ_0; all the models presented here take $\Sigma_0 = 10 \, M_\odot \, \mathrm{pc}^{-2}$.

In general, $\dot{M}$ would be large if the gas orbits near the center were highly eccentric or radial, while circular orbits would make $\dot{M}$ quite small. This expectation is consistent with Figure 18 which plots the temporal evolution of the mass inflow rates for all models. The corresponding accreted gas mass $M_{\mathrm{acc}} = \int \dot{M}(t)dt$ over 500 Myr is given in Table 5. Clearly, $\dot{M}$ is larger for models with larger c_s and no BH, compared to models with a massive BH
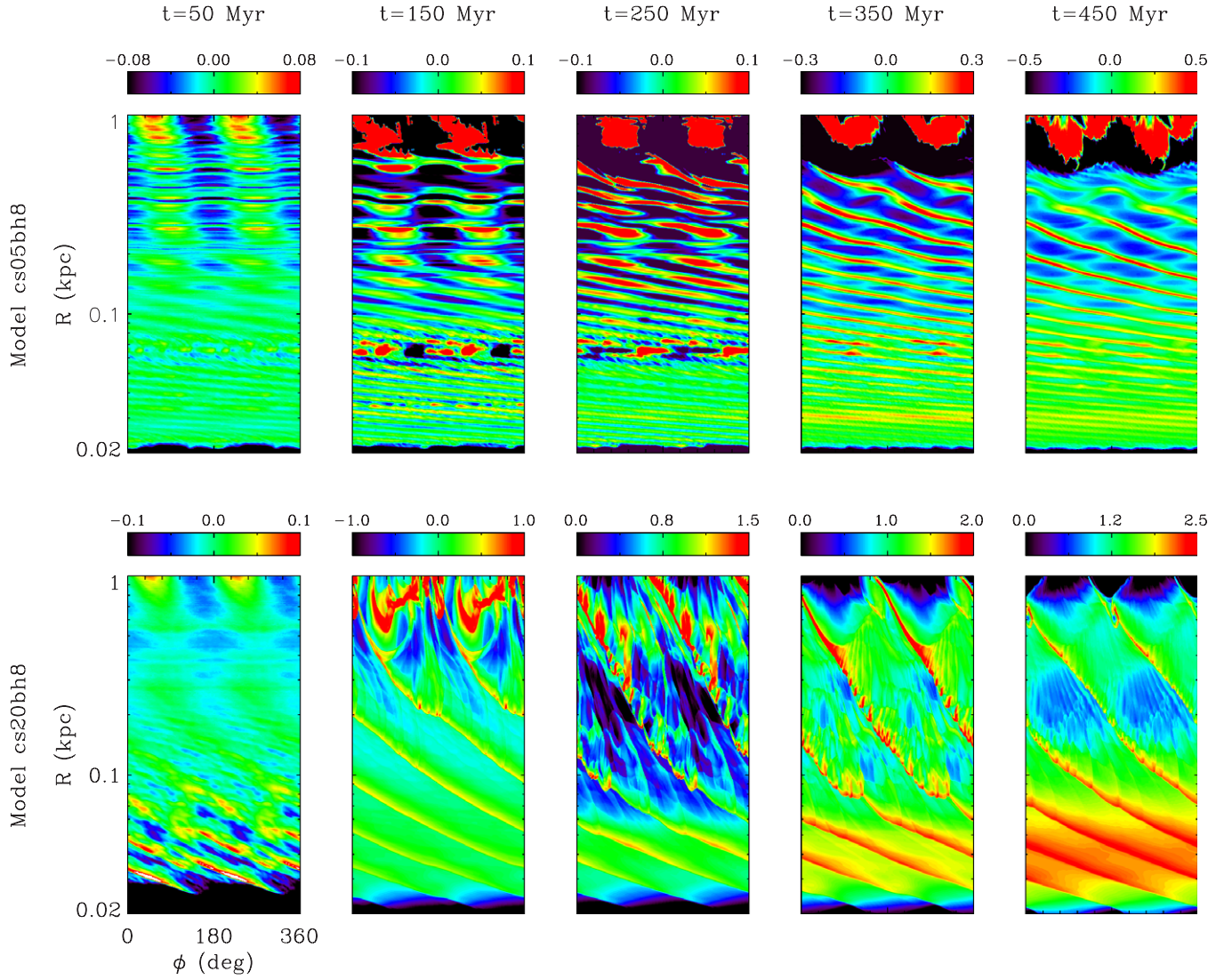
Figure 16. Snapshots of the logarithm of the gas surface density on the $\phi - \log R$ plane for Models cs05bh8 (top row) and cs20bh8 (bottom row). These models have a central BH with a mass of $4 \times 10^8\ M_\odot$. Only the regions with $R \leqslant 1$ kpc are shown.

(A color version of this figure is available in the online journal.)

Table 5
Total Mass of Gas Inflow at $t = 500$ Myr

Model	$M_{\rm acc}$ ($M_\odot$)
cs05bh0	8.9×10^4
cs05bh0t	1.1×10^5
cs10bh0	8.0×10^5
cs15bh0	2.7×10^6
cs20bh0	1.8×10^7
cs20bh0t	2.3×10^7
cs05bh7	4.2×10^4
cs10bh7	1.6×10^6
cs15bh7	7.4×10^6
cs20bh7	3.2×10^7
cs20bh7t	2.9×10^7
cs05bh8	9.4×10^3
cs10bh8	4.5×10^4
cs15bh8	2.0×10^5
cs20bh8	5.1×10^6

of $M_{\rm BH} = 4 \times 10^8\ M_\odot$. When $c_s = 5$ km s^{-1}, the nuclear spirals are well separated from the nuclear rings, and the departure of the gas orbits from a circular shape near the inner boundary is small, resulting in quite small values of $\dot{M}$ ($\lesssim 10^{-3}\ M_\odot$ yr^{-1}). In bh8 models, the presence of a central BH makes $\dot{M}$ smaller by about an order of magnitude than in bh0 models by providing strong axisymmetric gravitational potential near the center. In bh7 models, the BH potential is not strong enough to circularize the eccentric orbits, giving rise to $\dot{M}$ only slightly smaller than that in bh0 models.

Increasing c_s enhances $\dot{M}$ because pressure perturbations become stronger and the nuclear ring tends to be located closer to the center, both of which strongly affect the gas orbits in the central region. When $c_s = 10$ km s^{-1}, $\dot{M}$ is increased by about an order of magnitude compared to the cases with $c_s = 5$ km s^{-1}, but is still less than $10^{-2}\ M_\odot$ yr^{-1} except for a brief time interval around $t = 300$ Myr in Model cs10bh7 when the nuclear spirals shock the central gas and cause enhanced inflows. When $c_s \geqslant 15$ km s^{-1}, the gas orbits in bh0 and bh7 models are quite eccentric near the center, so that some gas with highly radial orbits plunges directly into the inner

17
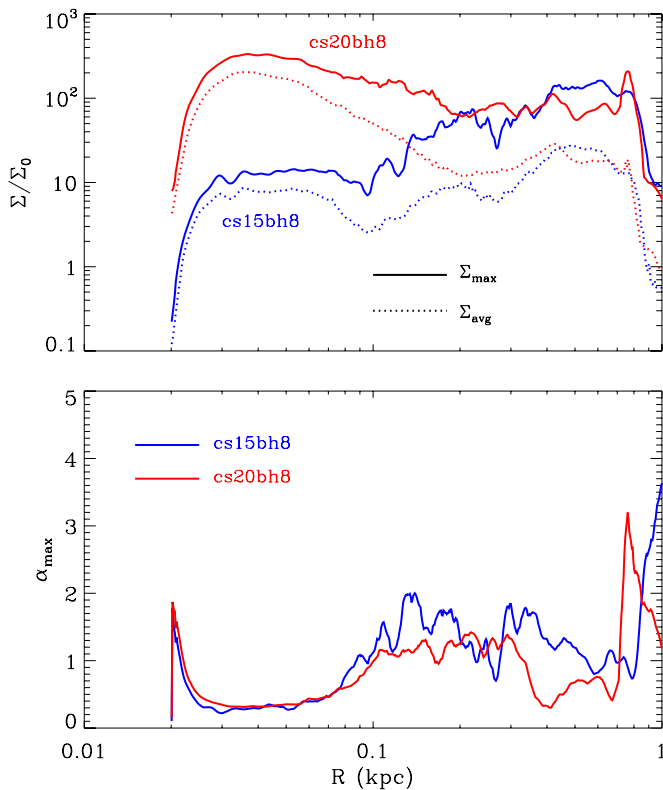
Figure 17. Radial distributions of the maximum and mean densities (top) and the maximum compression factor (bottom) in the inner 1 kpc regions of Models cs15bh8 and cs20bh8 at $t = 500$ Myr. Due to strong spiral shocks, the ring material in Model cs20bh8 is already moved to the $R \sim 0.02$–0.1 kpc region, while with weaker shocks it still lies at $R > 0.1$ kpc in Model cs15bh0. In both models, the shocks at $R \sim 0.05$ kpc are quite weak with the compression factor of $\alpha \sim 0.3$.

(A color version of this figure is available in the online journal.)

boundary, increasing $\dot{M}$ dramatically compared to the lower c_s counterparts. The associated gas mass accreted to the galaxy center is of the order of $\sim 10^7$ $M_\odot$ over 500 Myr, suggesting that a strong galactic bar as studied in this work can be an appealing means for the growth of supermassive BHs provided the gaseous medium has a large (effective) sound speed (see Shlosman et al. 1989; see also, e.g., Volonteri 2010 for a review). In bh8 models, on the other hand, the gas orbits in the central parts are not greatly perturbed (since the initial angular momentum is overwhelmingly large). As the nuclear spirals grow into shocks, however, the nuclear gas as well as the ring material in these models drifts slowly inward, increasing $\dot{M}$ over time. In models with $M_{BH} = 4 \times 10^8$ $M_\odot$, the late-time values of $\dot{M}$ in models with $c_s = 15$ or 20 km s^{-1} are larger than 0.01 $M_\odot$ yr^{-1}, sufficient to power AGNs in Seyfert galaxies (e.g., Friedli & Benz 1993; Fabian et al. 2008).

Finally, we present the mass inflow rates resulting from the models in which M_{BH} is varied self-consistently with $\dot{M}$. The left panels of Figure 19 compare $\dot{M}$ from Models cs05bh0t and cs20bh0t with those from the fixed-M_{BH} counterparts, while the bottom panels plot the temporal evolution of the BH mass in the former models. In Model cs05bh0t, the total gas mass accreted over 500 Myr is $\sim 10^5$ $M_\odot$, with the corresponding increment of the equilibrium rotational velocity of ~ 4 km s^{-1} at the inner boundary. Since this is three times smaller than the initial circular velocity there, the BH mass does not greatly affect $\dot{M}$, as Figure 19 illustrates. In the case of Model cs20bh0t, M_{BH}

attains $\sim 2 \times 10^7$ $M_\odot$ at $t = 500$ Myr, which is large enough to be dynamically important. When $c_s = 20$ km s^{-1}, however, the gas orbits are highly eccentric and $\dot{M}$ is insensitive to the BH mass as long as $M_{BH} \lesssim 4 \times 10^7$ $M_\odot$ (see Figure 18(d)). As the right panels of Figure 19 show, the increase of M_{BH} over 500 Myr in Model cs20bh7t is less than a factor of two, corresponding to the equilibrium circular velocity 1.3 times the initial value. With an enhanced centrifugal barrier, the resulting $\dot{M}$ becomes gradually smaller than the case with fixed M_{BH}, but by less than, on average, $\sim 10\%$ in $t = 300$–500 Myr. Therefore, we conclude that the effect of BH growth due to gas accretion on the mass inflow rate as well as bar substructures is not significant for the models we have considered.

## 6. SUMMARY AND DISCUSSION

6.1. Summary

We have presented detailed numerical models that explore the formation of substructures produced by the gas flow in barred galaxies. Previous models based on particle simulations (e.g., Englmaier & Gerhard 1997; Ann & Thakur 2005; Thakur et al. 2009) did not have sufficient resolution to resolve nuclear spirals. On the other hand, studies that used the grid-based code CMHOG (e.g., Piner et al. 1995; Maciejewski 2004b) unknowingly made mistakes in the force evaluation for the bar potential, so that the results needed to be recomputed.

In this paper, we have corrected the errors in the original CMHOG code and run high-resolution hydrodynamical simulations. To resolve the nuclear regions, we employed a logarithmically spaced cylindrical grid, with a zone size of $\Delta R \lesssim 6$ pc at $R \lesssim 1$ kpc where nuclear rings and spirals form. We have included the potential from a central BH and studied the flow properties as the mass of the BH M_{BH} and the sound speed c_s in the gas are varied. For simplicity, the effects of gaseous self-gravity and magnetic fields are not included. The main results of the present work are summarized as follows.

1. *Off-axis shocks*. The imposed non-axisymmetric bar potential provides gravitational torques to the otherwise circular-rotating gas, perturbing its orbit. The perturbed orbits crowd at the downstream sides of the bar major axis and produce over-dense ridges that eventually develop into off-axis shocks. At a quasi-steady state, the off-axis shocks are overall almost parallel to x_1-orbits: they start from the bar major axis at the outer ends, are gradually displaced downstream as they move inward, and connect to the nuclear ring at the inner ends. While the positions of the off-axis shocks are almost independent of M_{BH}, since the effect of a BH is negligible at large radii, they depend on c_s in such a way that the shocks are, on average, located closer to the bar major axis as c_s increases. This is primarily because gas with larger c_s should be more strongly perturbed to induce shocks, which occurs deeper in the potential well and thus results in shocks on lower x_1-orbits (Englmaier & Gerhard 1997).

The off-axis shocks are in general curved. Flow streamlines are complicated near the shocks in that they diverge before the shocks and are promptly swept inward by inflowing gas right after the shocks. Therefore, the usual Rankine–Hugoniot jump conditions for planar, one-dimensional shocks are not applicable to the off-axis shocks. In fact, the shock strength, as measured by the peak density Σ_{max} at $R \sim 1.5$–1.8 kpc from the center, is $\Sigma_{max}/\Sigma_0 \sim 3$–6 for models with no BH and does not sensitively depend on c_s. The compression factor of the off-axis shocks is insensitive to the BH mass and depends on c_s roughly as $\alpha_{max} \sim 7.7(c_s/5 \text{ km s}^{-1})^{0.92}$. The off-axis shocks have very
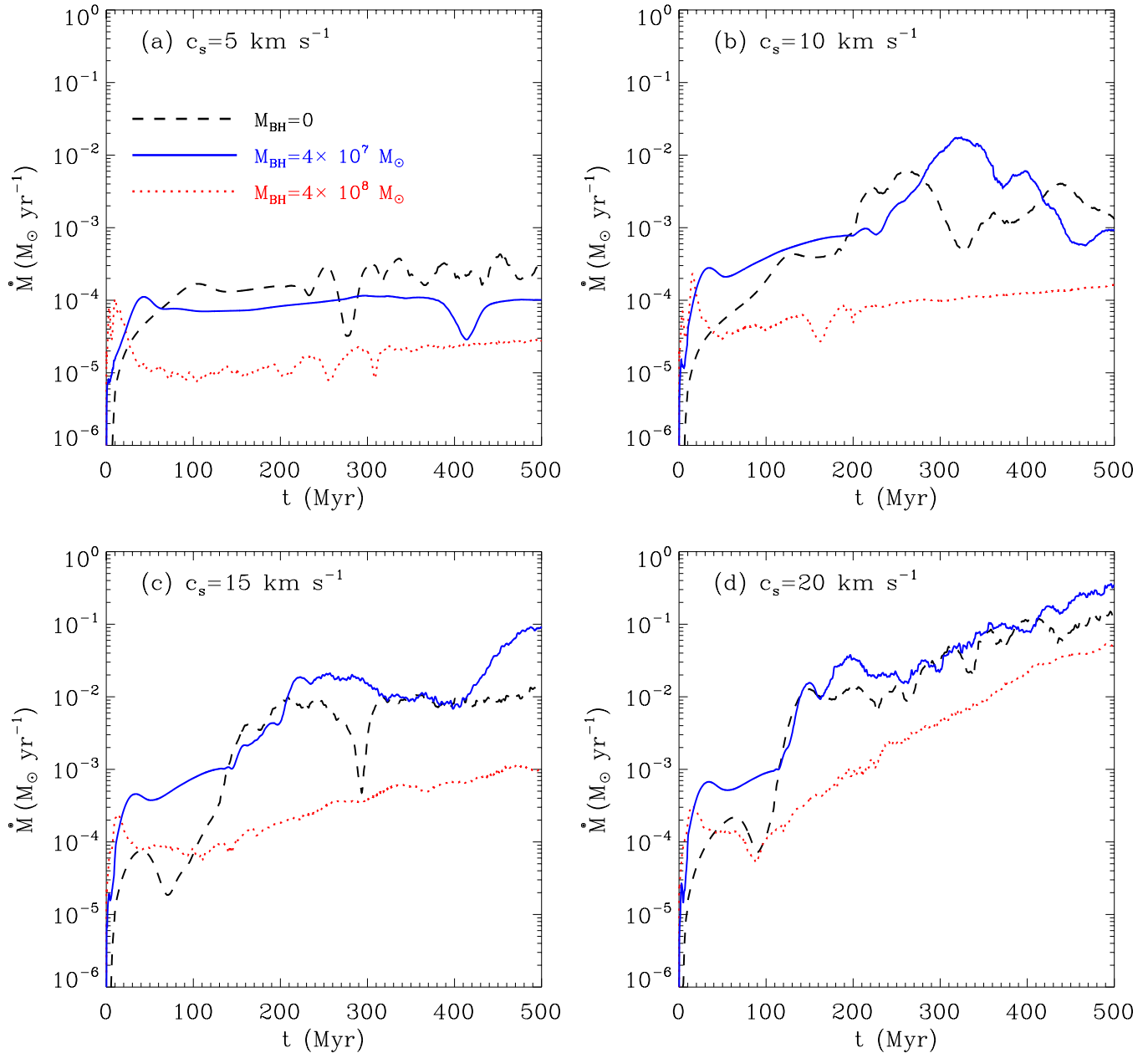
Figure 18. Temporal evolution of the mass inflow rates $\dot{M}$ through the inner boundary at $R = 20$ pc for models with (a) $c_s = 5$ km s^{-1}, (b) $c_s = 10$ km s^{-1}, (c) $c_s = 15$ km s^{-1}, and (d) $c_s = 20$ km s^{-1}. The dashed, solid, and dotted lines correspond to the cases with $M_{BH} = 0$, $4 \times 10^7\ M_\odot$, and $4 \times 10^8\ M_\odot$, respectively. (A color version of this figure is available in the online journal.)

strong velocity shear amounting to $\sim(1-3) \times 10^3$ km s^{-1} kpc^{-1}. This strong shear may suppress the growth of gravitational instability in the high-density off-axis shocks when self-gravity is included.

2. *Nuclear rings*. When gas passes through the off-axis shocks, it loses angular momentum, flows inward, and forms a nuclear ring where the centrifugal force balances the external gravity. The ring is attached to the inner ends of the off-axis shocks and thus becomes smaller in size as c_s increases. The rings that form in our models are all located inside the (outer) ILR, but this does not imply that the ring formation is related to the ILRs. When c_s is small, the pressure perturbations on the gas orbits are so weak that the rings are quite narrow and their shape is well described by x_2-orbits. The mean radius is $R_{ring} \sim 0.8-0.9$ kpc when $c_s = 5$ km s^{-1} and

$R_{ring} \sim 0.5-0.6$ kpc when $c_s = 10$ km s^{-1}, independent of the BH mass. This suggests that the ring position is not determined by the $\Omega - \kappa/2$ curve, hence by the ILRs. When $c_s \geqslant 15$ km s^{-1}, on the other hand, large thermal pressure strongly affects the gas orbits in the nuclear rings. For example, some gas near the contact points between the ring and the off-axis shocks is forced out to follow relatively round orbits, while other gas is pulled in radially to make very eccentric orbits. These diverse gas orbits near the contact points tend to spread out the ring material, making the rings much broader than in models with smaller c_s.

3. *Nuclear spirals*. Since even the non-axisymmetric bar potential is nearly axisymmetric in the central parts, the gaseous responses inside a nuclear ring are not as dramatic as in off-axis shocks. Nevertheless, non-axisymmetric $m = 2$ perturbations are able to grow inside a ring and develop into nuclear spirals
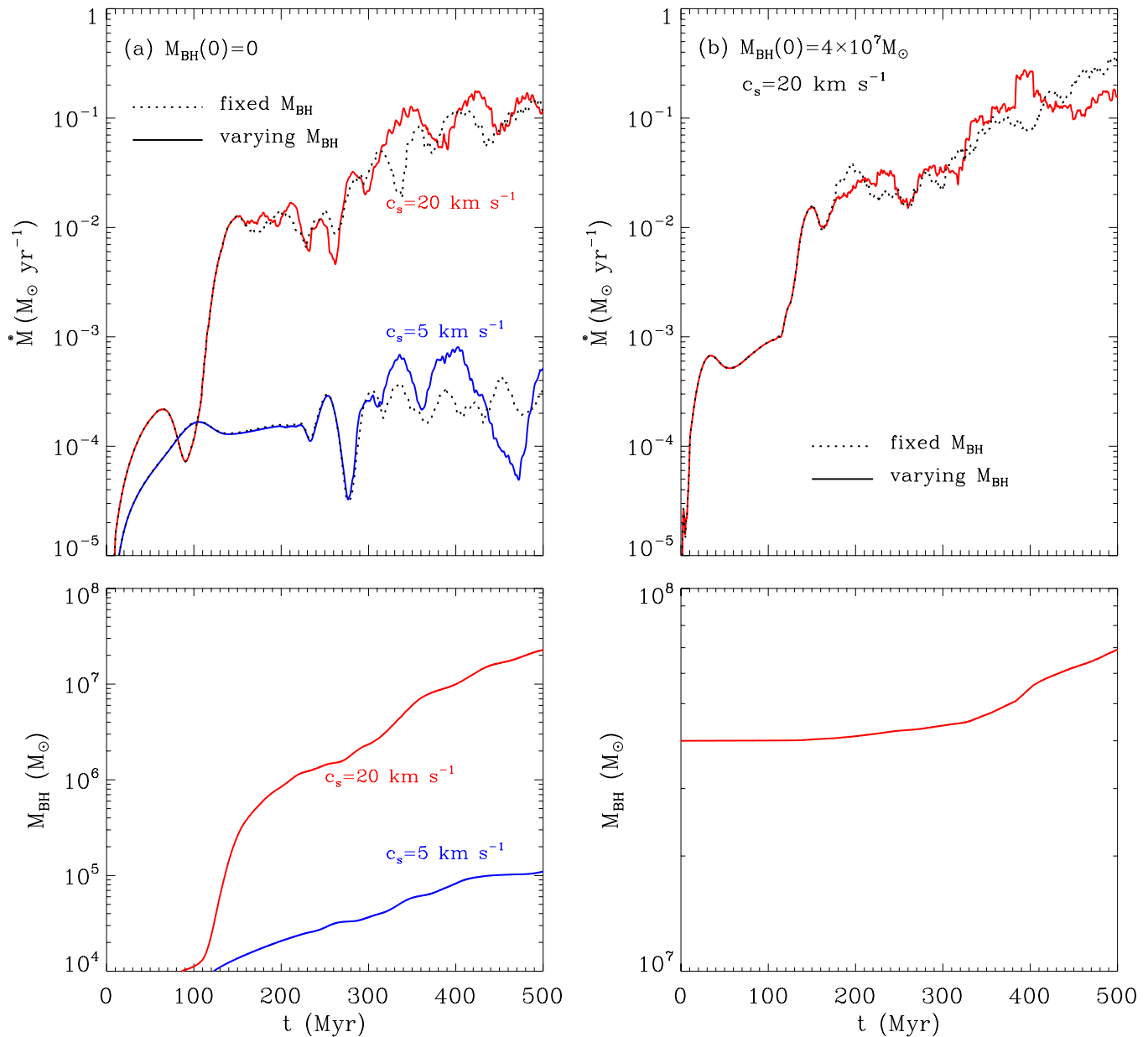
Figure 19. Temporal evolution of the mass inflow rates (top) and the BH mass (bottom) in Models cs05bh0t, cs20bh0t, and cs20bh7t, where $M_{\rm BH}$ is allowed to vary with time. The mass inflow rates from the fixed-$M_{\rm BH}$ counterparts are compared as dotted lines. In all models, the total increase in the BH mass over 500 Myr is not large enough to cause significant changes in $\dot{M}$.

(A color version of this figure is available in the online journal.)

that persist for a long period of time, provided that c_s is small or $M_{\rm BH}$ is large. Although all models have weak spiral structures at early time, in models with large c_s they are soon destroyed by eccentric gas orbits as well as perturbations induced by the large pressure in the rings unless the BH mass is very large. When $M_{\rm BH} = 4 \times 10^8 \, M_\odot$, the disruptive pressure perturbations from the rings cannot penetrate the very central parts where the gas has extremely large initial angular momentum. In this case, the nuclear spirals are protected from the surrounding and thus are long-lived.

The shape of nuclear spirals is determined by the sign of $d(\Omega - \kappa/2)/dR$ such that spirals that form in the regions where $d(\Omega - \kappa/2)/dR$ is positive (negative) are leading (trailing), confirming the theoretical expectations of Buta & Combes (1996). With no BH, only the model with $c_s = 5$ km s^{-1} has persistent leading spirals in the regions where the $\Omega - \kappa/2$ curve

is an increasing function of R. The leading spirals in this model are quite strong and develop into shocks with the peak density $\Sigma_{\rm peak}/\Sigma_{\rm avg} \sim 7.9$ and the compression factor $\alpha \sim 3.4$ at $R = 0.25$ kpc at the end of the run. Models with $M_{\rm BH} = 4 \times 10^7 \, M_\odot$ initially have hybrid features comprising trailing spirals at $R < R_{\rm min}$ and leading spirals at $R_{\rm min} < R < R_{\rm max}$, where $R_{\rm min}$ and $R_{\rm max}$ refer to the radii where the $\Omega - \kappa/2$ curve attains a local minimum and maximum, respectively. When $c_s \leqslant 10$ km s^{-1}, however, the leading parts in the hybrid spirals are destroyed by the trailing pressure waves launched by the ring, leaving only the weak trailing spirals behind. When $c_s \geqslant 15$ km s^{-1}, both leading and trailing spirals are destructed completely by the pressure perturbations. In models with $M_{\rm BH} = 4 \times 10^8 \, M_\odot$, $d(\Omega - \kappa/2)/dR < 0$ in the whole nuclear regions, so that nuclear rings are always trailing. When $c_s \leqslant 10$ km s^{-1}, the spirals well separated from the ring are weak and tightly

wound. When $c_s \geqslant 15$ km s^{-1}, on the other hand, the trailing spirals are fed by the gas in the nuclear ring and grow into shocks, the outer ends of which join the inner ends of the off-axis shocks smoothly. Although the nuclear spirals in these models have only modest density contrasts of $\Sigma_{\rm peak}/\Sigma_{\rm avg} \sim 1.7$ at $R = 0.05$ kpc, the background density resulting from the inflows of the ring material is greatly enhanced (by more than two orders of magnitude when $c_s = 20$ km s^{-1}).

4. *Mass inflow rates.* Although gas experiences a significant loss in angular momentum when it meets off-axis shocks during galaxy rotation, this does not necessarily translate into the mass inflow all the way to the galaxy center. In models with $c_s \leqslant 10$ km s^{-1}, a narrow nuclear ring formed by gas with x_2-orbits inhibits further inflows of the gas, resulting in the mass inflow rate $\dot{M}$ through the inner boundary less than 0.01 $M_\odot$ yr^{-1}, regardless of the BH mass. The mass inflow rates are greatly enhanced to $\dot{M} > 0.01$ $M_\odot$ yr^{-1} in models with $M_{\rm BH} \leqslant 4 \times 10^7$ $M_\odot$ and $c_s \geqslant 15$ km s^{-1} or $M_{\rm BH} = 4 \times 10^8$ $M_\odot$ and $c_s = 20$ km s^{-1} for different reasons depending on the BH mass. When $M_{\rm BH} \leqslant 4 \times 10^7$ $M_\odot$, the gas orbits are affected by thermal pressure and some gas in the ring can take highly eccentric orbits, directly falling into the inner boundary. In models with $M_{\rm BH} = 4 \times 10^8$ $M_\odot$, on the other hand, the gas orbits near the center are more or less circular, but the density in the nuclear regions is greatly enhanced because of strong nuclear spirals, increasing $\dot{M}$.

6.2. Discussion

Nuclear rings play an important role in the evolution of barred galaxies by providing sites of active star formation near the centers (e.g., Buta 1986; Garcia-Barreto et al. 1991; Barth et al. 1995; Maoz et al. 2001; Mazzuca et al. 2008). Rings certainly consist of gas that migrates from outer parts inward by losing angular momentum at off-axis shocks, but what stops further migration to form a ring remains a matter of debate. As a trapping mechanism of the ring material, Combes (1996) proposed the non-axisymmetric bar torque that forces gas to accumulate between two ILRs or at a single ILR depending on the shape of the gravitational potential (see also Buta & Combes 1996), while Regan & Teuben (2003, 2004) favored the gas transitions from x_1- to x_2-orbits rather than orbital resonances. However, our numerical results show that a ring is formed at early time because of the centrifugal barrier that the migrating material feels. Later on, nuclear rings slowly shrink in size as gas with lower angular momentum gas is continuously added. Although nuclear rings are located in between two ILRs in models with no BH, this is a coincidence. Models with a central BH show that the specific ring positions are insensitive to the shape of the $\Omega - \kappa/2$ curves, suggesting that nuclear ring formation is not a consequence of the orbital resonances. In fact, the gas flows that produce the ring are not in force balance and have a large radial velocity, so that the concept of resonances and ILRs is not applicable to nuclear rings (e.g., Regan & Teuben 2003). In addition, the notion of x_2-orbits as the gas trapping locations is meaningful only for small c_s.[13] When the sound speed is large, thermal pressure at the contact points between the off-axis shocks and nuclear ring causes the gas orbits to deviate from x_2-orbits considerably.

The results of our simulations suggest that not all barred galaxies possess nuclear spirals at their centers. Long-lasting

nuclear spirals exist only when either the sound speed is small or the BH mass is large: they do not survive in models with *both* large c_s *and* small $M_{\rm BH}$. Two common views regarding the nature of nuclear spirals are low-amplitude density waves and strong gaseous shocks (see, e.g., Englmaier & Shlosman 2000; Maciejewski et al. 2002; Maciejewski 2004a, 2004b; Ann & Thakur 2005; Thakur et al. 2009). And our simulations indeed show that they are either tightly wound density waves or shocks when the pitch angle is relatively large ($i_p > 6^\circ$). One may speculate that nuclear spirals are more likely to be shocks rather than density waves when c_s is small. In contrast to this prediction, however, nuclear spirals in models with $M_{\rm BH} = 4 \times 10^8$ $M_\odot$ are density waves when c_s is small and shocks when c_s is large. This is of course because as c_s increases, waves in nuclear regions tend to be more open (with smaller $|k|$) in the beginning, and they are subsequently supplied with more gas from the rings as they grow. This is entirely consistent with the results of Ann & Thakur (2005) who used SPH simulations to show that nuclear spirals are supported by shocks when $c_s \gtrsim 15$ km s^{-1} in models with a massive BH. We note however that weak trailing spirals seen in our Model cs10bh8 are absent in Model M2 ($c_s = 10$ km s^{-1} and $M_{\rm BH} = 4 \times 10^8$ $M_\odot$) of Ann & Thakur (2005), which is presumably due to an insufficient number of particles to resolve nuclear spirals in their SPH simulations.

Of 12 models with differing c_s and $M_{\rm BH}(0)$ that we have considered, only 1 model possesses leading spirals, suggesting that galaxies with leading nuclear spirals would be very uncommon in nature. To our knowledge, only two galaxies, NGC 1241 and NGC 6902, are known to possess leading features in the nuclear regions (Díaz et al. 2003; Grosbøl 2003).[14] Based on our simulations, the existence of leading spirals at centers requires two stringent conditions: (1) the gas should be dynamically cold enough to protect nuclear spirals from nuclear rings and (2) there should be a wide range of radii with $d(\Omega - \kappa/2)/dR < 0$ in the central parts, which can easily be accomplished when there are two ILRs (or without a strong central mass concentration). The second condition is consistent with the linear theory that predicts short leading waves propagating outward from the inner ILR (Maciejewski 2004a). The facts that NGC 6902 is a barred-spiral galaxy (Laurikainen et al. 2004) and does not show significant X-ray emissions indicative of AGN activities (Desroches & Ho 2009) are not inconsistent with the second requirement for the existence of leading nuclear spirals. Since NGC 1241 is a Seyfert 2 galaxy with an estimated BH mass of $\log(M_{\rm BH}/ M_\odot) = 7.46$ (Bian & Gu 2007), however, the nuclear star-forming regions in this galaxy are unlikely to be associated with gaseous nuclear spirals studied in this work.

Finally, we discuss the mass inflow rates derived in our models in regard to powering AGNs in Seyfert galaxies. The mass accretion rate is often measured by the Eddington ratio defined by $\lambda \equiv L_{\rm bol}/L_{\rm Edd} = 4.5 \times 10^{-2}(\epsilon/0.1)(\dot{M}/10^{-2}\ M_\odot\ {\rm yr}^{-1})(M_{\rm BH}/10^7\ M_\odot)^{-1}$, where $L_{\rm bol}$ and $L_{\rm Edd}$ denote the bolometric and Eddington luminosities of an AGN and ϵ is the mass-to-energy conversion efficiency of the accreted material. Observations indicate that $\lambda \lesssim 0.1$ for classical Seyfert 1 galaxies with broad iron emission lines (e.g., Meyer-Hofmeister & Meyer 2011; see also Peterson 1997), while $\lambda \sim 10^{-3}$ for low-luminosity Seyfert 1 AGNs (e.g., Ho

---

[13] The models considered by Regan & Teuben (2003, 2004) had the sound speed fixed to $c_s = 5$ km s^{-1}.

[14] Leading arms in NGC 1241 are detected by Paα emissions tracing young stars, while those in NGC 6902 are observed in the K' band tracing old populations. It is uncertain how these stellar features are related to gaseous nuclear spirals studied in this paper.

2008). In our numerical models, the mass inflow rates are larger for models with smaller M_{BH} and larger c_s. Taking $\epsilon \approx 0.1$ (e.g., Yu & Tremaine 2002), the mass inflow rates amount to $\lambda \lesssim 10^{-4}$ for $M_{BH} = 4 \times 10^8 \ M_\odot$ and $c_s \lesssim 15$ km s^{-1}, $\lambda \sim 10^{-3}$ for $M_{BH} = 4 \times 10^8 \ M_\odot$ and $c_s = 20$ km s^{-1} or for $M_{BH} = 4 \times 10^7 \ M_\odot$ and $c_s = 10$ km s^{-1}, and $\lambda \sim 0.02$–0.4 for $M_{BH} = 4 \times 10^7 \ M_\odot$ and $c_s \gtrsim 15$ km s^{-1}. For classical Seyfert galaxies with strong bars, this suggests that the masses of central BHs are likely to be less than $10^8 \ M_\odot$, which appears to be consistent with the measured values from the relation between the BH masses and the velocity dispersions of stellar bulges (e.g., Watabe et al. 2008) and reverberation mapping techniques (e.g., Gültekin et al. 2009; Denney et al. 2010). Of course, this result may depend on many factors such as the axis ratio and strength of the bar, presence of self-gravity and magnetic fields, gas cooling and heating, turbulence, etc., all of which would affect gas dynamic significantly. Extending the present work to include these physical ingredients would be an important direction of future research.

APPENDIX

THE GALAXY MODEL

In this appendix, we describe the gravitational potential of the model galaxy that maintains the rotation of the (non-self-gravitating) gas disk. The potential is comprised of four components: a stellar disk, a bulge, a bar, and a BH. For the disk, we take a Kuzmin–Toomre model with surface density

$$\sigma(R) = \frac{v_0^2}{2\pi G R_0}\left(1 + \frac{R^2}{R_0^2}\right)^{-3/2}, \tag{A1}$$

where v_0 and R_0 are constants (Kuzmin 1956; Toomre 1963). The corresponding gravitational potential at the disk midplane is

$$\Phi_{disk} = -\frac{v_0^2 R_0}{\sqrt{R^2 + R_0^2}}, \tag{A2}$$

(Binney & Tremaine 2008). We take $v_0 = 260$ km s^{-1} and $R_0 = 14.1$ kpc in our simulations.[15] The total disk mass is $M_{disk} = v_0^2 R_0/G = 2.2 \times 10^{11} \ M_\odot$.

For the bulge, we use a modified Hubble profile with volume density

$$\rho(R) = \rho_{bul}\left(1 + \frac{R^2}{R_b^2}\right)^{-3/2}, \tag{A3}$$

and the potential

$$\Phi_{bul} = -\frac{4\pi G \rho_{bul} R_b^3}{R}\ln\left(\frac{R}{R_b} + \sqrt{1 + \frac{R^2}{R_b^2}}\right), \tag{A4}$$

where ρ_{bul} and R_b are the central density and the characteristic size of the bulge, respectively. We take $\rho_{bul} = 2.4 \times 10^{10} \ M_\odot$ kpc^{-3} and $R_b = 0.33$ kpc, with the corresponding bulge mass of $M_{bul} = 2.8 \times 10^{10} \ M_\odot$ within $R = 6$ kpc.

The bar is modeled by a Ferrers (1887) ellipsoid with volume density

$$\rho = \begin{cases} \rho_{bar}(1 - g^2)^n & \text{for } g < 1, \\ 0 & \text{elsewhere,} \end{cases} \tag{A5}$$

where ρ_{bar} is the bar central density, $g^2 = y^2/a^2 + (x^2 + z^2)/b^2$ with (x, y, z) being the Cartesian coordinates, and a and b are the semimajor and semiminor axes of the bar, respectively. The exponent n measures the central concentration of the bar density distribution. In this work, we fix the bar parameters to $n = 1$, $a = 5$ kpc, $b = 2$ kpc, and $\rho_{bar} = 4.5 \times 10^8 \ M_\odot$ kpc^{-3} for all models. The total mass of the bar is then $M_{bar} = 2^{2n+3}\pi ab^2 \rho_{bar}\Gamma(n+1)\Gamma(n+2)/\Gamma(2n+4) = 1.5 \times 10^{10} \ M_\odot$ and the bar quadrupole moment is $Q_m = M_{bar}a^2[1 - (b/a)^2]/(5+2n) = 4.5 \times 10^{10} \ M_\odot$ kpc^2, corresponding to a strong bar. When $n = 1$, the bar potential is given explicitly as

$$\begin{aligned}\Phi_{bar}(x, y, z) = &-\frac{\pi G ab^2 \rho_{bar}}{2} \\ &\times [W_{000} + x^2(x^2 W_{200} + 2y^2 W_{110} - 2W_{100}) \\ &+ y^2(y^2 W_{020} + 2z^2 W_{011} - 2W_{010}) \\ &+ z^2(z^2 W_{002} + 2x^2 W_{101} - 2W_{001})], \end{aligned} \tag{A6}$$

where the coefficients W_{ijk}'s are as defined in Pfenniger (1984). As the bar pattern speed, we choose $\Omega_b = 33$ km s^{-1} kpc^{-1} which places the CR at $R_{CR} = 6$ kpc.

Finally, for a central BH with mass M_{BH}, we use a Plummer potential

$$\Phi_{BH} = -\frac{GM_{BH}}{(R^2 + R_s^2)^{1/2}}, \tag{A7}$$

with the softening radius $R_s = 1$ pc. We take $M_{BH} = 0$, $4 \times 10^7 \ M_\odot$, and $4 \times 10^8 \ M_\odot$ to study the effects of the central mass concentration on the bar substructures. With $M_{BH} \ll M_{disk}, M_{bul}, M_{bar}$, the BH affects the rotation curve only in the very central regions (with $R \lesssim 0.5$ kpc). Figures 1 and 2 plot the rotational velocity for models with $M_{BH} = 4 \times 10^8 \ M_\odot$ and the angular frequency curves for all models, respectively.

---

[15] Our choice of the disk model is slightly different from that of Piner et al. (1995) in that they took $v_0 = 200$ km s^{-1} and a surface density profile that is singular at $R = 0$ (see their Equation (1)). Our adopted parameters nevertheless give the rotational curves similar to those shown in their Figure 1.

REFERENCES

Agertz, O., Moore, B., Stadel, J., et al. 2007, MNRAS, 380, 963
Ann, H. B., & Thakur, P. 2005, ApJ, 620, 197
Athanassoula, E. 1992a, MNRAS, 259, 328
Athanassoula, E. 1992b, MNRAS, 259, 345
Barth, J., Ho, C., Filippenko, V., & Sargent, W. L. 1995, AJ, 110, 1009
Bian, W., & Gu, Q. 2007, ApJ, 657, 159
Binney, J., & Tremaine, S. 2008, Galactic Dynamics (2nd ed.; Princeton, NJ: Princeton Univ. Press)
Buta, R. 1986, ApJS, 61, 609
Buta, R., & Combes, F. 1996, Fundam. Cosm. Phys., 17, 95
Colella, P., & Woodward, P. R. 1984, J. Comput. Phys., 54, 174
Combes, F. 1996, in ASP Conf. Ser. 91, Barred Galaxies, ed. R. Buta, D. A. Crocker, & B. G. Elmegreen (San Francisco, CA: ASP), 286
Contopoulos, G., & Grosbøl, P. 1989, A&AR, 1, 261
Denney, K. D., Peterson, B. M., Pogge, R. W., et al. 2010, ApJ, 721, 715
Desroches, L.-B., & Ho, L. C. 2009, ApJ, 690, 267
Díaz, R. J., Dottori, H., Vera-Villamizar, N., & Carranza, G. 2003, ApJ, 597, 860
Englmaier, P., & Gerhard, O. 1997, MNRAS, 287, 57

Englmaier, P., & Shlosman, I. 2000, ApJ, 528, 677
Fabian, A. C., Vasudevan, R. V., & Gandhi, P. 2008, MNRAS, 385, L43
Ferrers, N. M. 1887, Q. J. Pure Appl. Math., 14, 1
Field, G. B., Goldsmith, D. W., & Habing, H. J. 1969, ApJ, 155, L149
Friedli, D., & Benz, W. 1993, A&A, 268, 65
Garcia-Barreto, J. A., Downes, D., Combes, F., et al. 1991, A&A, 244, 257
Goldreich, P., & Tremaine, S. 1978, ApJ, 222, 850
Grosbøl, P. 2003, in Galaxies and Chaos, ed. G. Contopoulos & N. Voglis (Lecture Notes in Physics, Vol. 626; Berlin: Springer), 201
Gültekin, K., Richstone, D. O., Gebhardt, K., et al. 2009, ApJ, 698, 198
Heller, C. H., & Shlosman, I. 1994, ApJ, 424, 84
Ho, L. C. 2008, ARA&A, 46, 475
Kim, J., Ryu, D., Jones, T. W., & Hong, S. S. 1999, ApJ, 514, 506
Kim, W.-T., & Ostriker, E. C. 2006, ApJ, 646, 213
Knapen, J. H., Shlosman, I., & Peletier, R. F. 2000, ApJ, 529, 93
Kuzmin, G. 1956, Astron. Zh., 33, 27
Laurikainen, E., Salo, H., Buta, R., & Vasylyev, S. 2004, MNRAS, 355, 1251
Maciejewski, W. 2004a, MNRAS, 354, 883
Maciejewski, W. 2004b, MNRAS, 354, 892
Maciejewski, W., Teuben, P. J., Sparke, L. S., & Stone, J. M. 2002, MNRAS, 329, 502
Maoz, D., Barth, J., Ho, C., Sternberg, A., & Filippenko, V. 2001, AJ, 121, 3048
Martinez-Valpuesta, I., Shlosman, I., & Heller, C. 2006, ApJ, 637, 214
Martini, P., Regan, M. R., Mulchaey, J. S., & Pogge, R. W. 2003a, ApJS, 146, 353
Martini, P., Regan, M. R., Mulchaey, J. S., & Pogge, R. W. 2003b, ApJ, 589, 774
Mazzuca, L. M., Knapen, J. H., Veilleux, S., & Regan, M. W. 2008, ApJ, 174, 337
McKee, C. F., & Ostriker, E. C. 2007, ARA&A, 45, 565
McKee, C. F., & Ostriker, J. P. 1977, ApJ, 218, 148
Meyer-Hofmeister, E., & Meyer, F. 2011, A&A, 527, A127
Patsis, P. A., & Athanassoula, E. 2000, A&A, 358, 45
Peterson, B. M. 1997, An Introduction to Active Galactic Nuclei (Cambridge: Cambridge Univ. Press)
Pfenniger, D. 1984, A&A, 134, 373
Piner, B. G., Stone, J. M., & Teuben, P. J. 1995, ApJ, 449, 508
Price, D. J. 2008, J. Comput. Phys., 227, 10040
Prieto, M. A., Maciejewski, W., & Reunanen, J. 2005, AJ, 130, 1472
Read, J. I., Hayfield, T., & Agertz, O. 2010, MNRAS, 405, 1513
Regan, M. W., & Mulchaey, J. S. 1999, AJ, 117, 2676
Regan, M. W., & Teuben, P. J. 2003, ApJ, 582, 723
Regan, M. W., & Teuben, P. J. 2004, ApJ, 600, 595
Roberts, W., Huntley, M., & Van Albada, G. D. 1979, ApJ, 233, 67
Sanders, R. H., & Huntley, J. M. 1976, ApJ, 209, 53
Schwarz, M. P. 1981, ApJ, 247, 77
Shlosman, I., Begelman, M. C., & Frank, J. 1990, Nature, 345, 679
Shlosman, I., Frank, J., & Begelman, M. C. 1989, Nature, 338, 45
Springel, V., Yoshida, N., & White, S. D. M. 2001, New Astron., 6, 79
Thakur, P., Ann, H. B., & Jiang, I. 2009, ApJ, 693, 586
Toomre, A. 1963, ApJ, 138, 385
van Albada, G. D., & Roberts, W. W. 1981, ApJ, 246, 740
van de Ven, G., & Fathi, K. 2010, ApJ, 723, 767
Volonteri, M. 2010, A&AR, 18, 279
Wada, K., & Koda, J. 2004, MNRAS, 349, 270
Watabe, Y., Kawakatu, N., & Imanishi, M. 2008, ApJ, 677, 895
Yu, Q., & Tremaine, S. 2002, MNRAS, 335, 965
Yuan, C., & Yen, D. C. C. 2005, J. Korean Astron. Soc., 38, 197